Stem Cell Reports
Article

ISSCR

OPEN ACCESS

Cell-to-Cell Adhesion and Neurogenesis in Human Cortical Development: A Study Comparing 2D Monolayers with 3D Organoid Cultures

Soraya Scuderi,[1,5] Giovanna G. Altobelli,[1,2,5] Vincenzo Cimini,[2] Gianfilippo Coppola,[1,4,*] and Flora M. Vaccarino[1,3,*]

[1]Child Study Center, Yale University, New Haven, CT 06520, USA
[2]Advanced Biomedical Sciences Department, University "Federico II", Naples, Italy
[3]Department of Neuroscience, Yale University, 230 South Frontage Road, New Haven, CT 06520, USA
[4]Department of Pathology, Yale University, 310 Cedar Street, New Haven, CT 06520, USA
[5]These authors contributed equally
*Correspondence: gianfilippo.coppola@yale.edu (G.C.), flora.vaccarino@yale.edu (F.M.V.)
https://doi.org/10.1016/j.stemcr.2020.12.019

SUMMARY

Organoids (ORGs) are increasingly used as models of cerebral cortical development. Here, we compared transcriptome and cellular phenotypes between telencephalic ORGs and monolayers (MONs) generated in parallel from three biologically distinct induced pluripotent stem cell (iPSC) lines. Multiple readouts revealed increased proliferation in MONs, which was caused by increased integrin signaling. MONs also exhibited altered radial glia (RG) polarity and suppression of Notch signaling, as well as impaired generation of intermediate progenitors, outer RG, and cortical neurons, which were all partially reversed by reaggregation of dissociated cells. Network analyses revealed co-clustering of cell adhesion, Notch-related transcripts and their transcriptional regulators in a module strongly downregulated in MONs. The data suggest that ORGs, with respect to MONs, initiate more efficient Notch signaling in ventricular RG owing to preserved cell adhesion, resulting in subsequent generation of intermediate progenitors and outer RG, in a sequence that recapitulates the cortical ontogenetic process.

INTRODUCTION

Induced pluripotent stem cells (iPSCs), generated by somatic cell reprogramming (Takahashi et al., 2007; Yu et al., 2007), hold considerable promise for fundamental biological studies into early human brain development (Ardhanareeswaran et al., 2017; Arlotta and Pasca, 2019; Sidhaye and Knoblich, 2021). In general, two models have been used to achieve *in vitro* neuronal differentiation. In the first, iPSCs are used to generate neuroepithelial progenitor cells (NPCs) that are then dissociated into single cells and differentiated into neurons in monolayer (MON) preparations (Chambers et al., 2009; Shi et al., 2012). In the second, NPCs grow and differentiate in the context of organoid (ORG) structures in three-dimensional (3D) conditions (Camp et al., 2015; Eiraku et al., 2008; Lancaster et al., 2013; Mariani et al., 2012, 2015).

MONs are a simpler way to differentiate human neurons, but these cells are not able to segregate in layers and compartments as occurs in normal development, and the underlying mechanism of this failure is not known. In contrast, ORG preparations have a spontaneous self-organizing ability to form a neuroepithelium layer where cell polarity, membrane contacts, and morphogen gradients are maintained. Under appropriate culture conditions, proliferating progenitors within ORGs sequentially generate early- and late-born cortical neurons as well as glial cells. A key difference between MON and ORG preparations is differential contact between cells and the extracellular matrix (ECM), which are processes that are known to affect a variety of cellular behaviors, including cell growth, differentiation, and motility (Engler et al., 2006; Saha et al., 2008). Yet, differences in stem cell differentiation abilities under MON and 3D conditions have not been directly compared. Here, we analyze the effects of cell dissociation into MONs versus continuous growth in 3D conditions upon the processes that lead human iPSCs to differentiate into telencephalic neurons. To avoid confounds created by differences in genetic background and reprogramming methods, three iPSC lines were differentiated into neurons as ORGs or MONs in parallel and exposed to identical culture media and conditions. Immunocytochemical, transcriptome, and proteome analyses revealed enduring, long-term differences in neuron specification and differentiation among the two conditions. Reversal experiments reaggregating the MONs and culturing them under 3D conditions corrected excessive cell proliferation and some, but not all, differences in cell fate and gene expression between MONs and ORGs. By varying the timing of dissociation we also found that, while cell-to-cell contacts exert an enduring influence on regional specification and neuronal differentiation of human stem cell precursors, late dissociation seems to have less deleterious effects upon reaggregation.

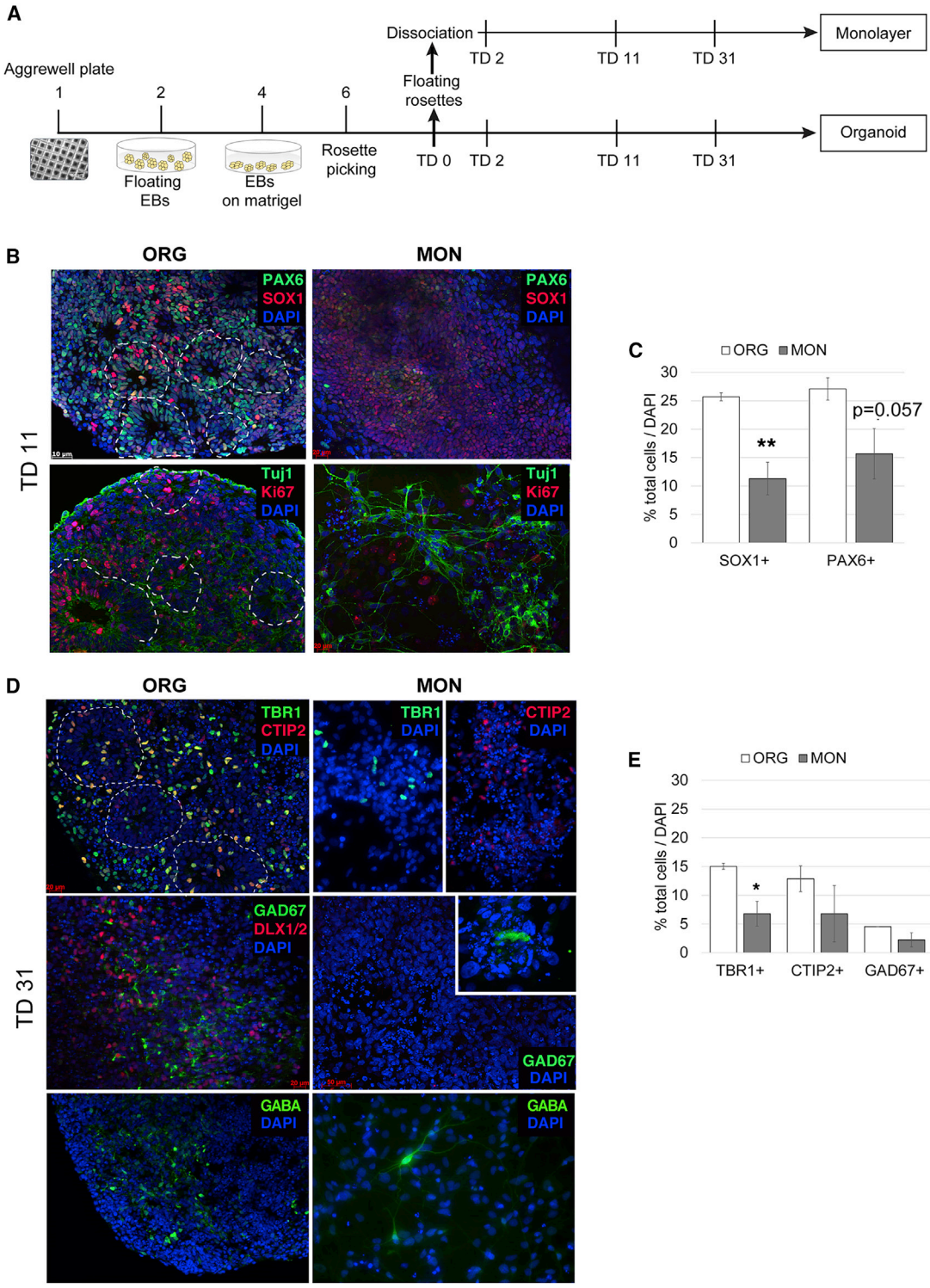

Figure 1. Comparison of 2D versus 3D *In Vitro* Cell Cultures

(A) Experimental design. TD, terminal differentiation day; EB, embryoid bodies; MON, monolayer; ORG, organoid.

(B) Representative images of immunocytochemical staining with the dorsal telencephalic marker PAX6, the neuroectodermal marker SOX1, the proliferative marker Ki67, and the neuron-specific class III β-tubulin at TD11.

(C) Proportion of $SOX1^+$ and $PAX6^+$ cells by stereological quantification over $DAPI^+$ nuclei.

(legend continued on next page)

RESULTS

Cell Dissociation and MON Culture Impact Cellular Organization and Fate

To understand how cell dissociation and the microenvironment might affect the emergence of cortical identity, we compared the transcriptome, proteome, and cell fate of three iPSC lines derived from adult control males differentiated in parallel under two separate conditions: undissociated ORG and MON cultures (Table S1).

Telencephalic ORGs were prepared (Mariani et al., 2015) using Noggin as neuralizing agent, by aggregating iPSCs into embryoid bodies (EBs), patterning the EBs by BMP, transforming growth factor β, and Wnt inhibition, and culturing the EB-derived neuroepithelium under 3D conditions. The MONs were prepared by dissociating the ORGs at terminal differentiation day 0 (TD0) (which is the day when ORGs are switched into mitogen-free medium) and plating the NPCs on plastic permanox slides coated with poly-L-ornithine-laminin. Both ORG and MON preparations were cultured in parallel in the same medium until analysis (Figure 1A).

After 11 days in terminal differentiation medium (TD11), the undissociated ORG preparation displayed layers of polarized radial glial (RG) cells expressing the cortical neural progenitor markers SOX1 and PAX6 (Figure 1B). The cell-cycle marker Ki67 was mostly located in the RG cell layer, with cells undergoing mitosis at the apical edge, whereas β3-tubulin$^+$ young neurons were located on the basal side of this layer. In MONs, cells were not polarized or organized into layers. The number of SOX1$^+$ RG cells in MONs was decreased as compared with ORGs (12% ± 3.49% in MONs versus 25% ± 0.69% in ORGs). A comparable trend was observed for PAX6 (Figure 1C). In conclusion, dissociation resulted in disorganized morphology and cellular architecture, with poor expression of RG markers when compared with undissociated ORGs.

On TD31, ORGs displayed a consistent ability to generate TBR1$^+$ (layer 6) and CTIP2$^+$ (layer 5) cortical neurons across the different lines, in agreement with previous results (Mariani et al., 2015). In contrast, the MONs displayed lower and highly variable counts of TBR1$^+$ and CTIP2$^+$ cortical neurons (Figures 1D and 1E). Similarly, we observed a lack of consistent GABAergic neuronal differentiation in MONs, as shown by very low levels of GAD1/GAD67 or GABA immunostaining, as opposed to a reproducible number of GAD67$^+$ inhibitory neurons (about 5% of all cells) in ORGs.

To assess differential proliferative activity, we immunostained ORGs and MONs for Ki67, a nuclear protein expressed only during cell division. At TD2, there were 45.65% ± 5.06% Ki67$^+$ in MONs compared with 19.69% ± 1.64% in ORGs; the increase was highly significant ($p < 0.001$) (Figure S1). At TD11, no significant differences in the number of Ki67$^+$ cells were observed between the conditions. These findings suggest a short-term proliferative effect induced by dissociation in the MON cultures.

Distinct Transcriptional Trajectories of ORG and MON Preparations

To study each system's individual developmental trajectory, we investigated the temporal evolution of the ORG and MON transcriptome at TD2, TD11, and TD30. For a list of differentially expressed genes (DEGs) across all transitions and their gene ontology (GO) and canonical pathway (CP) annotations (see Table S2).

At TD11 versus TD2, we identified 3,780 and 4,126 DEGs for ORG and MON conditions, respectively (Figure 2A). CP annotations for downregulated genes were mostly related to mitosis and cell cycle (e.g., cyclins *CDC2* and *CDC25*) for both ORGs and MONs (Figures 2C and 2D), reflecting the shared capability of escaping cell division for both systems. Top CP terms in ORGs for upregulated genes were related to synaptic formation and neurotransmitter release, synaptic vesicles, and calcium channel genes. In contrast, the top CP terms for upregulated genes in MONs were related to lysosome, intraflagellar transport, cilium formation, and ECM molecules and receptor interactions (e.g., *LAMA2* and *COL1A*).

At the second transition, TD31 versus TD11, we identified 1,175 and 296 DEGs for ORG and MON conditions, respectively (Figure 2B). Thus, the MON appears to be a relatively static condition, whereas the ORGs keep evolving transcriptionally. Notably, functional analysis of downregulated genes at this transition was still related to cell cycle in the MONs, whereas in ORGs they were related to neural crest differentiation (comprising a number of WNT pathway genes and WNT-targeted transcription factors [TFs]), Hippo signaling, and signaling pathways regulating pluripotency of stem cells (Figure 2E).

Relative expression levels across samples for 34 randomly selected human genes as revealed by RNA sequencing

(D) Immunocytochemical staining of excitatory (TBR1$^+$ and CTIP2$^+$) and inhibitory (GABA$^+$, GAD67$^+$) cortical neurons at TD31.
(E) Proportion of excitatory and inhibitory neurons over DAPI$^+$ nuclei assessed by stereological analysis. Results in (C and E) are the mean ± SEM of n = 3 biologically different iPSC lines per condition (ORG, MON) differentiated in parallel with two technical replicates per cell line.
**$p < 0.01$, *$p < 0.05$ Student's t test, two tailed. See also Figure S1.

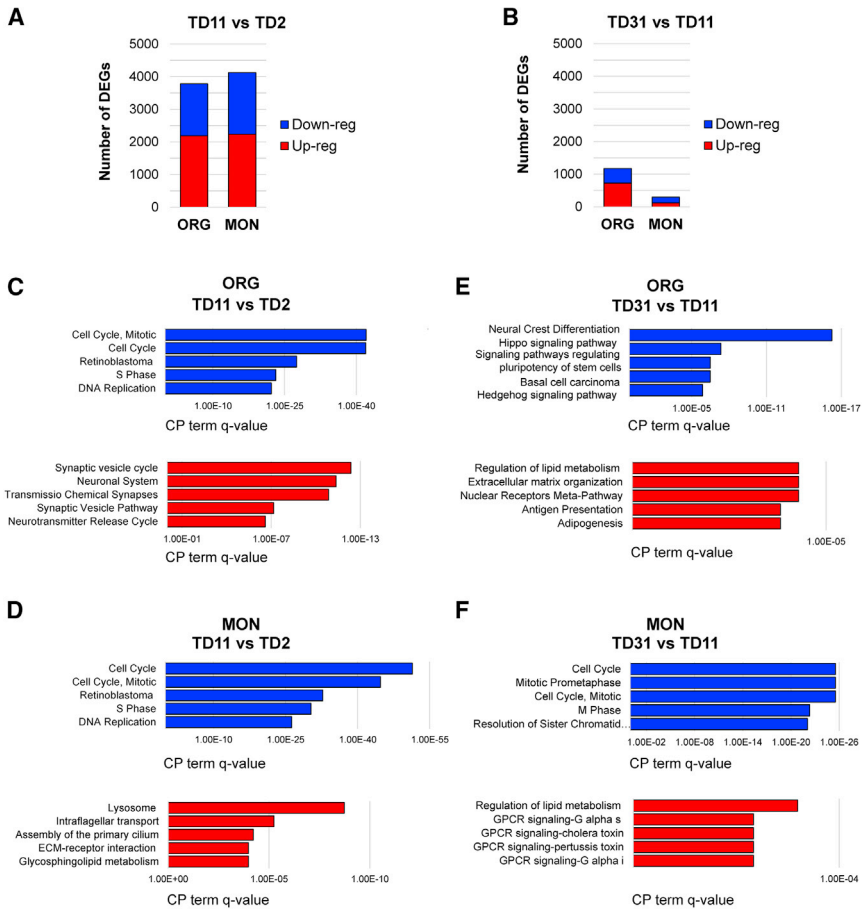

Figure 2. Longitudinal Differential Gene Expression Analysis in ORGs and MONs

(A and B) Number of differentially expressed genes (DEGs) at the first transition (TD11 versus TD2) (A) and at the second transition (TD31 versus TD11) (B) within each model. Blue, downregulated genes; red, upregulated genes.

(C–F) Canonical pathway (CP) term enrichment for genes upregulated (red) and downregulated (blue) per transition as indicated: (C and D) TD11 versus TD2; (E and F) TD31 versus TD11. The x axis indicates FDR-corrected p value in reverse order. For full annotation see Table S2. Results are from between two and three biologically different iPSC lines differentiated in parallel.

(RNA-seq) were generally concordant with those obtained by qRT-PCR of poly(A) RNA, thus validating the RNA-seq data (Table S3).

Collectively, the data suggest that ORGs downregulate pluripotency genes and WNT signaling to progressively differentiate into telencephalic neurons, with dynamic up- and downregulation of relevant genes, including neurotransmitter- and synapse-related genes and TFs, regulating cell fate, whereas the regional identity of the MON model is much less defined.

Telencephalic Patterning and Neuronal Fate Genes Are Downregulated in MON Cultures

Next, we compared differential gene expression between the isogenic MON and the ORG preparations at each time point, TD2, TD11, and TD31. The DEGs and their GO and CP annotations are listed in Table S3. ORG and the MON DEGs decreased with time (Figure 3A), suggesting a possible convergence of the two systems. More detailed analyses revealed that, whereas the majority of the DEGs present at TD2 were transient and not shared at later time points, 72% and 78% of the DEGs between MONs versus ORGs at TD31 were also present, respectively, at TD2 and TD11 (Figure 3B). In contrast, the relative number of strong transcriptional alterations (i.e., abs (log2 fold change) > 2) increased with time (Figure 3C), suggesting that MONs and ORGs evolve along divergent trajectories.

We next explored the biological identities of the two systems. For downregulated genes in MONs with respect to ORG, GO and CP enrichment analysis revealed similar top annotations at all time points, i.e., neuronal system, axon guidance, neurogenesis, and synaptic transmission. In contrast, top CP annotation terms for upregulated genes were cell cycle at TD2, and ECM organization and focal adhesion at both TD11 and TD31 (Figures 3D–3F).

To better understand these signatures, we constructed a manually curated list of genes which we call *Neurodevelopmental Genes* and subdivided it into relevant sublists according to specific criteria (see the Experimental Procedures): *Neuronal Cell Fate* (168 genes), *Cell Adhesion* (247 genes), *Axon Guidance* (175), and *Extracellular Matrix* (86 genes) (Tables S4A–S4D). Overall, 66% of genes in the

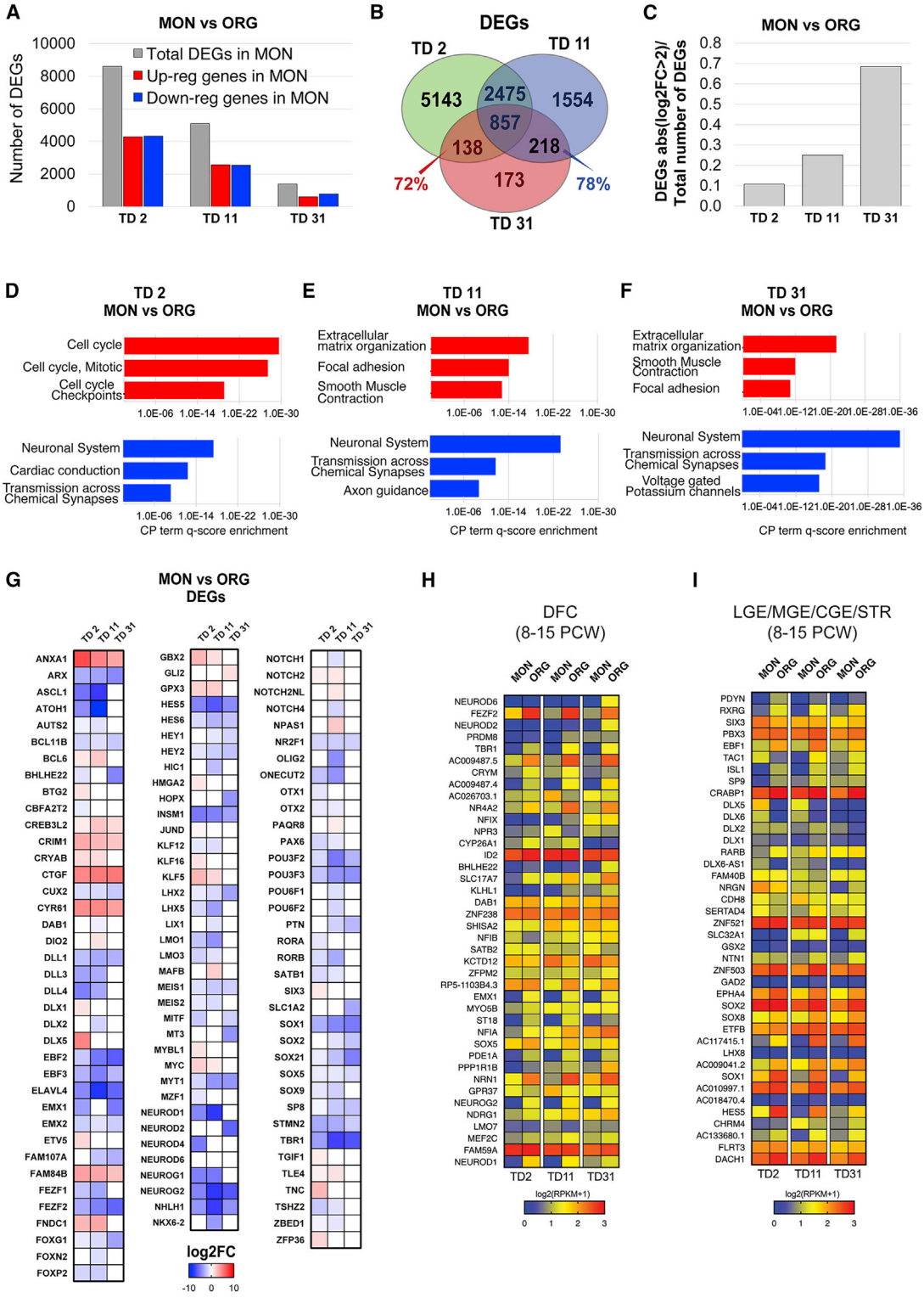

Figure 3. Comparison of MON and ORG Transcriptional Profiles at Three Different Stages of Neuronal Differentiation (TD2, TD11, and TD31)

(A) Total number of DEGs (gray bar), downregulated DEGs (blue bar), and upregulated DEGs (red bar) in MONs versus ORGs.

(B) Venn diagram of DEGs in MONs versus ORGs at each time point.

(legend continued on next page)

Neuronal Cell Fate sublist were downregulated in MONs versus ORGs (Figure 3G) at most of the time points considered. This is consistent with the failed upregulation of neuronal determinants in MONs, noted earlier in the longitudinal analysis. Interestingly, genes of the Notch pathway, which regulate neurogenesis from RG cells, were uniformly downregulated in MONs as compared with ORGs, including Notch ligands (*DLL1*, *DLL3*, and *DLL4*), Notch receptors (*NOTCH1* and *NOTCH4*), downstream transcriptional regulators (*HES5*, *HEY1* and *HEY2*), and downstream basic-helix-loop-helix neurogenic genes, which are the earliest determinants of dorsal and ventral telencephalic fates (*ASCL1*, *NEUROG1*, *NEUROG2*, *NEUROD1*, *NEUROD2*, *NEUROD4*, and *NEUROD6*). Among the genes significantly downregulated in MONs versus ORGs were a large number of homeodomain genes and other TFs that pattern the telencephalon (*LHX2*, *PAX6*, *EMX1*, *EMX2*, and *FOXG1*), specify pyramidal neuron fates (*TBR1*, *CTIP2*, and *POU3F2*) and GABAergic neuron fates (*ASCL1*, *DLX2*, and *FOXG1*) (Figure 3G).

We then examined differential gene expression in the *Cell Adhesion* sublist of genes, encompassing cell-to-cell adhesion molecules. A large spectrum of genes of the IgCAM family (e.g., *N-CAM* and *NCAM1*), cadherin and protocadherin (*CDH2*, *CDH22*, *CDH7*, and *PCDH10*), neurexins (*NRXN1*, *NRXN2*, and *NRXN3*), and contactin (e.g., *CNTN2* and *CNTN3*) superfamilies, were downregulated in the MONs versus ORGs at all time points, as well as genes in the *Axon Guidance* sublist, such as EPH/ephrins (Figures S2A, S2B, and S3A). By comparison with lists of genes that are expressed in the dorsal frontal cortex and basal telencephalon of human fetal brains (see the Experimental Procedures), ORGs exhibited a clear dorsal and ventral telencephalic signature, most evident at TD31, and no clear shift in fate was observed in MONs compared with ORGs (Figures 3H and 3I).

The very first cells that express neurogenic determinants in the developing cortex are RG daughter cells that delaminate from the apical layer to form the intermediate precursor cell (IPC) layer and the outer RG cell layer, which are much expanded in the human cortex (Johnson et al., 2015; Pollen et al., 2015). Hence, we further investigated the RG subtype composition in MONs and ORGs by examining the expression of key marker genes for various types of RG (Nowakowski et al., 2017) in our dataset. While we observed increased expression levels of some ventricular RG (vRG) transcripts (e.g., *ANXA1*, *CTGF*, and *CYR61*) and truncated RG (tRG) transcripts (*CRYAB* and *GPX3*) in the MONs compared with the ORGs, there was a strong downregulation of outer RG-specific transcripts (*FAM107A*, *HOPX*, *MT3*, and *PTN*) in MONs, particularly at the later time points (Figure S3C), suggesting failed evolution of neurogenic RG diversity and fate in MONs.

Increased Integrin Signaling in MON Cultures Triggers Cell Proliferation

Next, we examined DEGs in the *Extracellular Matrix* sublist of the curated *Neurodevelopmental Genes* list (Table S4D). In contrast to cell-to-cell adhesion molecules, there was a strong overexpression of major ECM components in MONs compared with ORGs (Figure S4A), which is concordant with top CP term enrichment for genes upregulated in MONs at both TD11 and TD31 (Figures 3E and 3F). This overexpression was most pronounced for laminins and integrins (e.g., *ITGA1*, *ITGA5*, *ITGB1*, *ITGB5*, and *ITGB6*). Integrins are αβ heterodimeric ECM receptors where β1 subunits (ITGβ1) form non-covalent complexes with many α subunits that bind laminin in the CNS (Milner and Campbell, 2002). Consistently, integrin signaling was strongly upregulated at both TD2 and TD11 in MONs, as compared with ORGs, by western blot analyses for phospho-FAK (p-FAK), an adherens junction protein that localizes at sites of integrin receptor accumulation and becomes phosphorylated at different tyrosine residues after engagement of integrin with ECM proteins (Figures 4A and 4B).

Integrin signaling has been involved in the proliferation of neural precursor cells (Long et al., 2016). To test the role of these ECM proteins in the regulation of neuronal stem cell and precursor behavior, we performed an independent experiment where we differentiated one iPSC line into MONs and ORGs with three separate technical replicates each. The MON cultures were treated with a monoclonal β1-integrin-blocking antibody that was previously demonstrated to block integrin function (Iba et al., 2000). In the majority of integrin receptor heterodimers, ITGβ1 is the major mediator of signaling pathways sensing

(C) Ratio between the number of highly differentially expressed genes (absolute value [log2 fold change > 2]) and the total number of DEGs in MONs versus ORGs along the time course.

(D–F) CP term enrichment for genes upregulated (red) and downregulated (blue) in MONs versus ORGs at each time point, TD2 (D), TD11 (E), and TD31 (F), with the FDR-corrected p value in reverse order on the x axis. For full annotation see Table S3.

(G) Heatmap displaying the log2 fold change values of transcripts from the *Neuronal Cell Fate* sublist (Table S4A) differentially expressed in MONs versus ORGs.

(H and I) Expression level (log2 (RPKM +1)) in MONs and ORGs of genes that are highly expressed in human dorsolateral prefrontal cortex (DFC) (H) versus basal telencephalon (lateral ganglionic eminence, medial ganglionic eminence, caudal ganglionic eminence, and striatum) or highly expressed in basal telencephalon versus DFC (I).

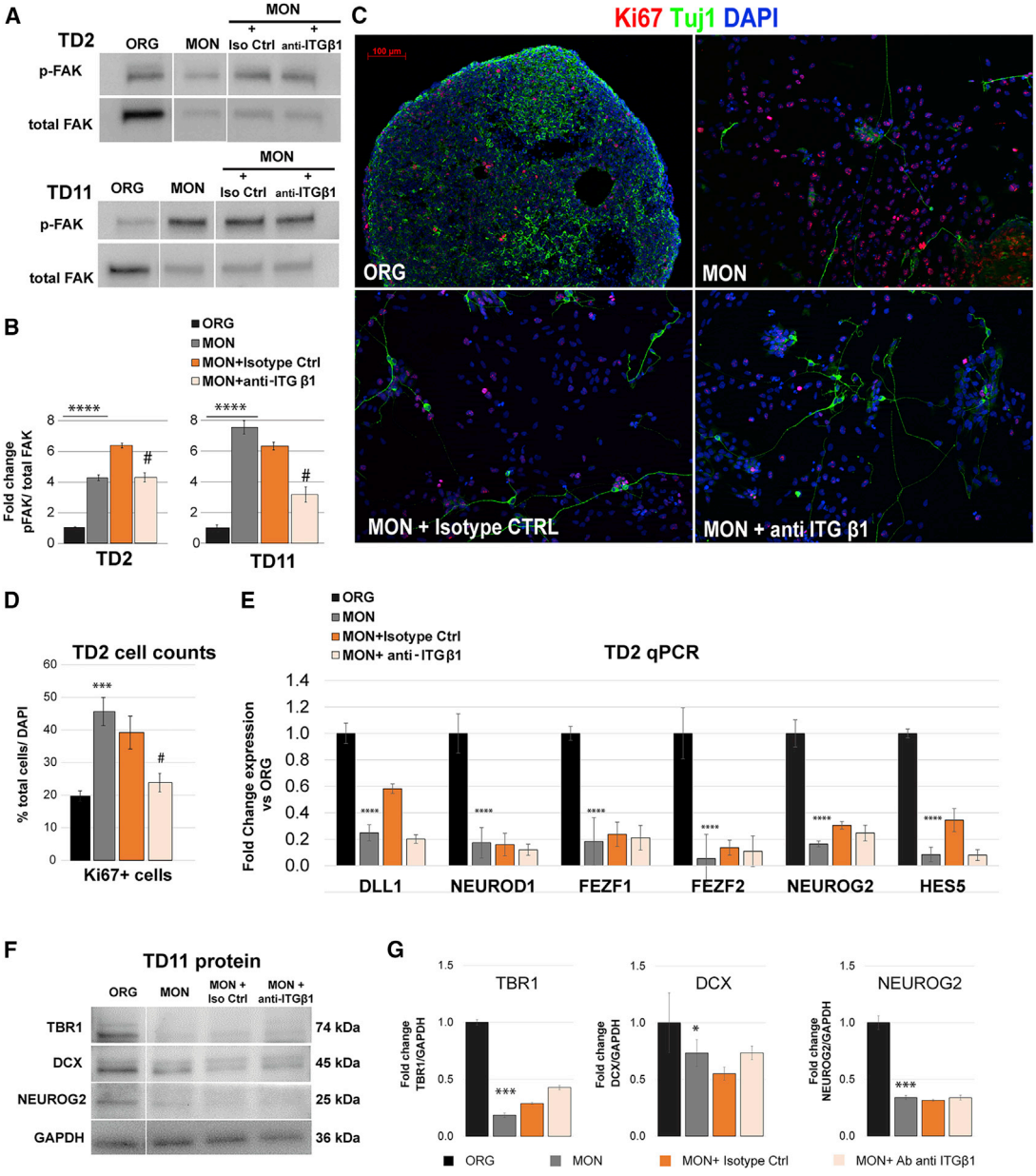

Figure 4. β1 Integrin Signaling Increases MON Cell Proliferation at Early Stages of Differentiation

(A and B) Western blot analysis (A) and quantification of protein expression level (B) of phospho-FAK in ORG, MON and MON treated with either an isotype control antibody (Iso Ctrl) or an anti-β1-integrin antibody (anti- β1ITG) at TD2 and TD11.

(C and D) Representative images (C) and stereological quantification (D) of immunostaining with the proliferative marker Ki67 and the neuron-specific marker TUJ1 at TD2 under the conditions described above.

(E) Relative expression level of a subset of genes from the *Neuronal Cell Fate* list (Table S4A) at TD2.

(F and G) Western blot analysis (F) and quantification of protein expression level (G) of TBR1, DCX, and NEUROG2 at TD11. GAPDH was used as loading control.

Data are expressed as mean ± SEM of n = 3 preparations per condition (ORGs or MONs with or without each antibody) from one iPSC line. *p < 0.05, ***p < 0.01, ****p < 0.001; MONs versus ORGs; #p < 0.05 MONs + anti-ITGβ1 versus MONs + Isotype Ctrl. One-way ANOVA with Tukey multiple comparisons test. See also Figure S4.

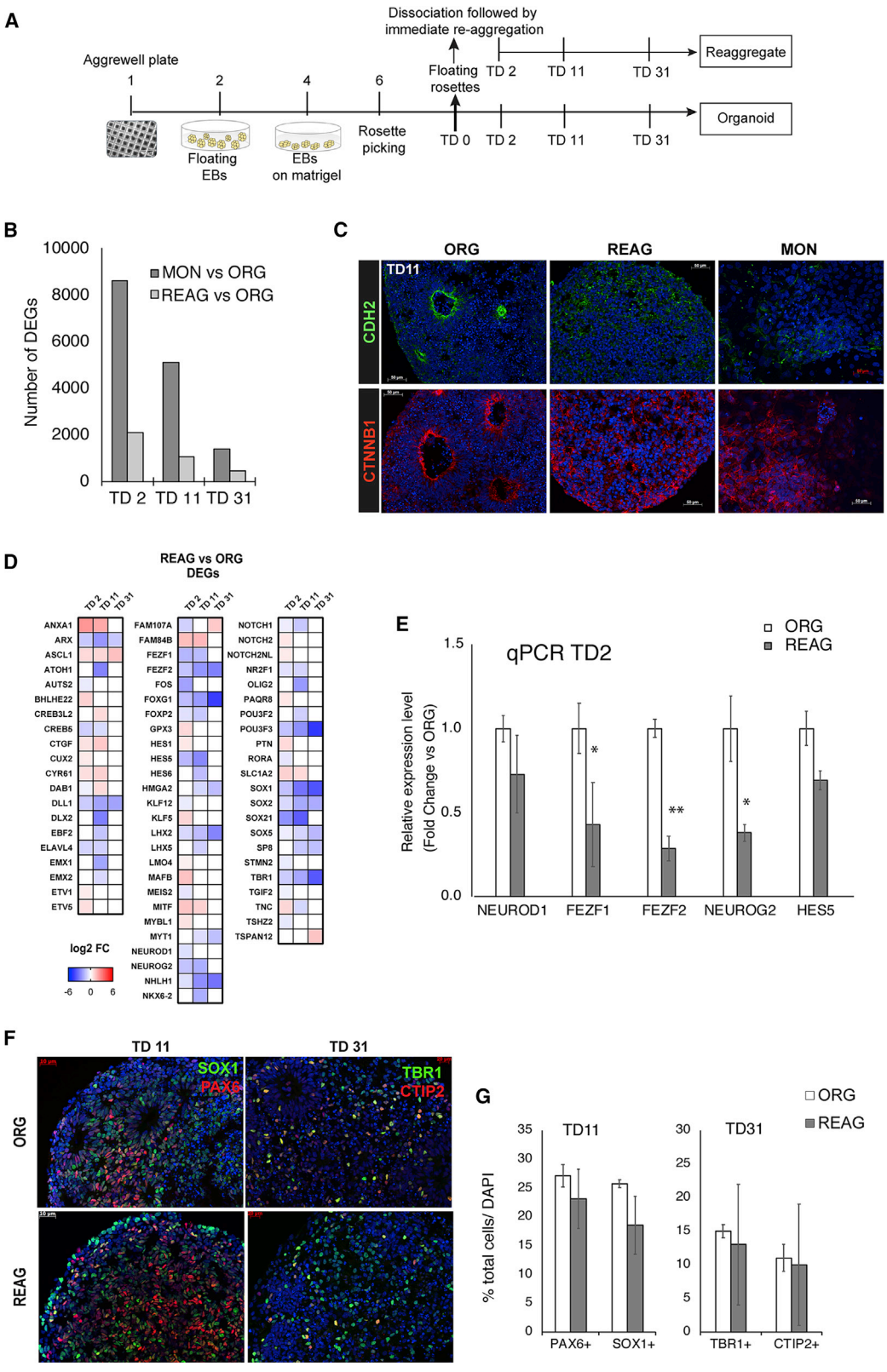

(legend on next page)

microenvironments rich in laminin. We first confirmed that the p-FAK protein level was decreased upon treatment of MON cultures with the anti-ITGβ1 antibody, both at TD2 and TD11 (Figures 4A and 4B), as compared with an isotype control antibody. We then assessed whether integrin blockade was able to revert the increased proliferation in MONs. As compared with the isotype control antibody condition, in which the number of proliferative cells was similar to that in medium alone (39.20% ± 2.84% and 45.65% ± 5.06%, respectively), blocking ITGβ1 at TD2 significantly reduced the percentage of proliferative cells in the MONs to values close to the ORG preparation (23.38% ± 0.9%) (Figures 4C and 4D).

To understand the potential effect of ITGβ1 signaling on neuronal differentiation, we then assessed levels of several cell fate- and neurogenesis-related transcripts by qPCR, whose expression levels were lower in MONs as opposed to the ORGs in the RNA-seq experiments. We confirmed that MONs had a several-fold decrease in the expression of *FEZF2*, *FEZF1*, *NEUROG2*, *NEUROD1*, *DLL1*, and *HES5* transcripts with respect to ORGs. However, the expression level of these transcripts did not change in the MONs as a consequence of blocking ITGβ1, either at the RNA or the protein level (Figures 4E–4G). Together, these data suggest that the increase in proliferation in MONs is triggered by integrin signaling, whereas the neurogenesis defect in MONs is not. Furthermore, the increased proliferation and decreased production of cortical neurons in the MON condition are independent from each other as they can be uncoupled by manipulating integrin signaling.

Differences in Neurogenic Cell Fate Are Partially Reversed by Reaggregation

We reasoned that decreased cortical neurogenesis in MONs could be attributable to decreased cell-to-cell contact, rather than increased cell-to-substrate adhesion. To assess whether cell-to-cell interactions per se were responsible for the failure of MONs to properly differentiate, we performed an experiment in which a portion of the dissociated NPCs were immediately re-aggregated and cultured in 3D in parallel to the MON and ORG preparations, using the same TD medium. We call this preparation a re-aggregated culture (REAG) (Figure 5A).

We then compared the transcriptomes of REAGs and ORGs (the lists of DEGs, and their GO and CP annotations, are shown in Table S5). In comparison to MONs versus ORGs, the number of DEGs at TD2 and TD11 was much less pronounced in REAGs versus ORGs (Figure 5B). However, the number of DEGs at TD30 were comparable with those in MON versus ORG preparations, and functional enrichment analysis of the DEGs in REAGs versus ORGs still revealed similar top GO and CP annotations as for the DEGs in MONs versus ORGs, i.e., neurogenesis and neuronal differentiation. Interestingly, in the *Extracellular Matrix* sublist, 66% of the genes were differentially expressed in MONs versus ORGs and only 24% in REAGs versus ORGs (Figures S4A and S4B; Table S4D), suggesting that the overexpression of ECM transcripts noted in MONs were partly compensated by reaggregation. Correspondingly, no changes in FAK phosphorylation were noted in the REAG versus ORG comparison (Figures S4C–S4F). Confirming the causal relationship between integrin signaling and cell proliferation, the increase in cell proliferation previously noted in MONs versus ORGs was no longer evident when REAG cultures were compared with ORGs (19.69% ± 1.64% in ORGs and 20.24% ± 4.31% in REAGs at TD2, Figure S1). Hence, the prompt reaggregation after dissociation prevents the upregulation in ITG signaling as well as other dissociation-induced short-term transcriptional alterations.

IgCAM family members (cadherin and protocadherin) were also partially restored under the REAG conditions. In the *Cell Adhesion* sublist, 51% of the genes were differentially expressed in MONs versus ORGs and only 20% in REAGs versus ORGs (Figures S2A–S2D). However, immunocytochemical analyses showed mislocalization of N-cadherin (CDH2) protein to a similar extent in both MONs and REAGs, as compared with ORGs where CDH2 is strictly localized in the apical RG cell feet (Figure 5C). This mislocalization was concomitant with a partial disruption in cell

Figure 5. Dissociation followed by Immediate Reaggregation

(A) Experimental design.

(B) Number of DEGs, at each time point, for the comparisons REAGs versus ORGs and MONs versus ORGs.

(C) Representative images of immunocytochemical staining for N-cadherin (CDH2, green) and β-catenin (CTNNB1, red) at TD11 in ORG, REAGs, and MON preparations ($DAPI^+$ nuclei in blue).

(D and E) Heatmap showing the log2 fold change (D) and bar graph of mRNA expression level by qPCR (E) of DEGs from the *Neuronal Cell Fate* gene sublist (Table S4A).

(F and G) Representative images of immunocytochemical staining with neuronal progenitor markers (PAX6, SOX1), and the excitatory cortical neuron markers TBR1 and CTIP2 (F) with proportion of different cell types assessed by stereological analysis (G). Results of RNA-seq analysis are from n = 2 biologically different iPSC lines per condition (ORG, REAG) differentiated in parallel.

Immunocytochemical data are expressed as mean ± SEM of n = 3 biologically different iPSC lines per condition (ORG, REAG). Two technical replicates per cell line were analyzed. $^{**}p < 0.01$, $^{*}p < 0.05$, MONs versus ORGs analyzed by t test, two tailed. See also Table S5.

polarity of the neuroepithelium and a lack of segregation between layers of dividing progenitors and postmitotic neurons. The apical-basal polarity loss after dissociation was confirmed by absence of β-catenin at the apical endfeet of RG in both REAGs and MONs (Figure 5C). Progenitor cells did express SOX1 and PAX6, but the RG layer was thinner as compared with the ORG preparation, with TBR1$^+$, CTIP2$^+$, and β3-tubulin$^+$ neurons dispersed throughout rather than being excluded from the RG progenitor layer (Figures 5F and S1). There appeared to be some improvement in cortical cell fate with respect to MONs, as the number of DEGs in the *Neuronal Cell Fate* sublist was 66% in MONs versus ORGs and only 35% in REAGs versus ORGs (Figure 5D, Table S4A). In addition there was a recovery in expression of axon guidance transcripts (Figures S3A and S3B) and outer RG gene markers in REAGs (Figures S3C and S3D). However, the expression of some Notch-related transcripts (*NOTCH1*, *DLL1*, and *HES5*), telencephalic neurogenic genes (*NEUROG2* and *NEUROD1*), and key telencephalic cell fate genes, such as *FOXG1*, *LHX2*, *FEZF1/2*, *EMX1*, *TBR1*, and *EOMES*, were still downregulated in REAGs versus ORGs, both by RNA-seq and qPCR (Figures 5D and 5E). Immunocytochemical characterization of the REAG cultures revealed persistent variability in cortical cell fate, as determined by counts of cortical neuron precursors expressing the layer-specific TFs TBR1 and CTIP2 (Figures 5F and 5G). Although without ultrastructural data we cannot ensure total restoration of membrane contacts, the data suggest that not cell adhesion per se, but proper orientation and polarity of cell-to-cell contacts, which was not entirely restored in the REAGs, must be responsible for persistent neurogenic defects in REAG preparations.

Gene Network Analyses Suggest Relationships between Cell Adhesion and Cell Fate

To obtain additional insights into the proposed interplay between cell-to-cell adhesion molecules and disruption of neural cell fate, we applied weighted gene co-expression network analysis (WGCNA) (Langfelder and Horvath, 2008) to the full set of MON and ORG samples. We identified 42 co-expression modules (Table S5A), all of which survived robustness testing. We found that 35 of the 42 modules are enriched in DEGs for MONs versus ORGs at one or more time points (Table S6B), and seven modules (*blue*, *brown*, *orange*, *purple*, *red*, *turquoise*, and *yellow*) are strongly enriched in DEGs at all three time points (more than 20 genes and false discovery rate [FDR] < 0.05). Among those, the *blue*, *brown*, *orange*, and *yellow* are enriched in DEGs mostly downregulated in MONs, whereas the *purple*, *red*, and *turquoise* are enriched in DEGs mostly upregulated in MONs (Figure 6A). Most of the modules downregulated in MONs were annotated by neuronal functions. The *blue* module was enriched in neurogenesis and cell adhesion GO terms, with most differentially expressed proneural, neurogenic genes, cadherins, and protocadherins clustered in this module, suggesting a relationship between cell adhesion and neurogenesis (Tables S6E and S6F). The *brown* module was enriched in synaptic genes; while the *orange* and *yellow* modules were enriched in DNA binding, RNA metabolism, and transcriptional regulation. Notch ligands, receptors, and downstream molecules clustered in both the *blue* (*RFNG*, *RBPJ*, *MAML3*, *DLL3*, *DLL4*, *MFNG*, *NOTCH4*, and *DTX1*) and *yellow* (*MAML1*, *HEYL*, *DLL1*, *NOTCH1*, *HES5*, *HES6*, *DTX4*, and *NEURL1B*) modules. In contrast, the three modules upregulated in MONs displayed non-neuronal annotations: the *purple* module was enriched in actin, focal adhesion, and ECM, with most of the differentially expressed ITG receptors clustered into this module; the *turquoise* module was enriched in cell-cycle and DNA replication terms, and the *red* module was enriched in peptide and vesicle transport (Figure S5A; Tables S6C and S6D). Module eigengene analysis can provide a simplified global picture of the system. Consistently with enrichment in DEGs, the *blue*, *brown*, *orange*, and *yellow* modules showed higher eigengene expression in ORGs, and the *purple*, *red*, and *turquoise* showed higher expression in MONs (Figure 6B). Correlation analysis between module eigengenes showed positive correlation between the *orange*, *blue*, and *yellow* modules and a negative correlation between the *purple* and those in the *blue* and *orange* modules (Figure 6C). To explore the mechanism of these relationships, we performed TF analysis using the Enrichr online database (see the Experimental Procedures) for the genes in each module and identified a set of putative TF-target gene pairs. At the network level, we find that TFs upstream of genes in the *blue* module belong to the *blue*, *orange*, and *yellow* modules, indicating that the strong positive correlations among these modules may represent, at least *in silico*, TF-target regulatory relationships. Focusing on the *blue* module and its putative TFs, we filtered out upstream TFs whose targets were not in the list of DEGs at any time points, resulting in a set of 60 TFs regulating the *blue* module (Table S7A). Among these, 41 TFs targeted both cell adhesion- and neurogenesis-related genes (Table S7B), and, among those, 12 (*MYT1*, *INSM1*, *ZSCAN18*, *SCRT1*, *EBF3*, *DPF1*, *MEIS3*, *UNCX*, *NEUROD4*, *ZNF536*, *ST18*, and *DEAF1*) were co-expressed with their targets in the *blue* module (Figure 6D; Table S7C). Interestingly, 11 out of these 12 TFs are downregulated in MONs versus ORGs at least at one time point. The co-expression of these TFs and their targets within the same module support a regulatory relationship, suggesting that this set of TFs is at least in part responsible for downregulating cell adhesion and neurogenic genes in MONs.

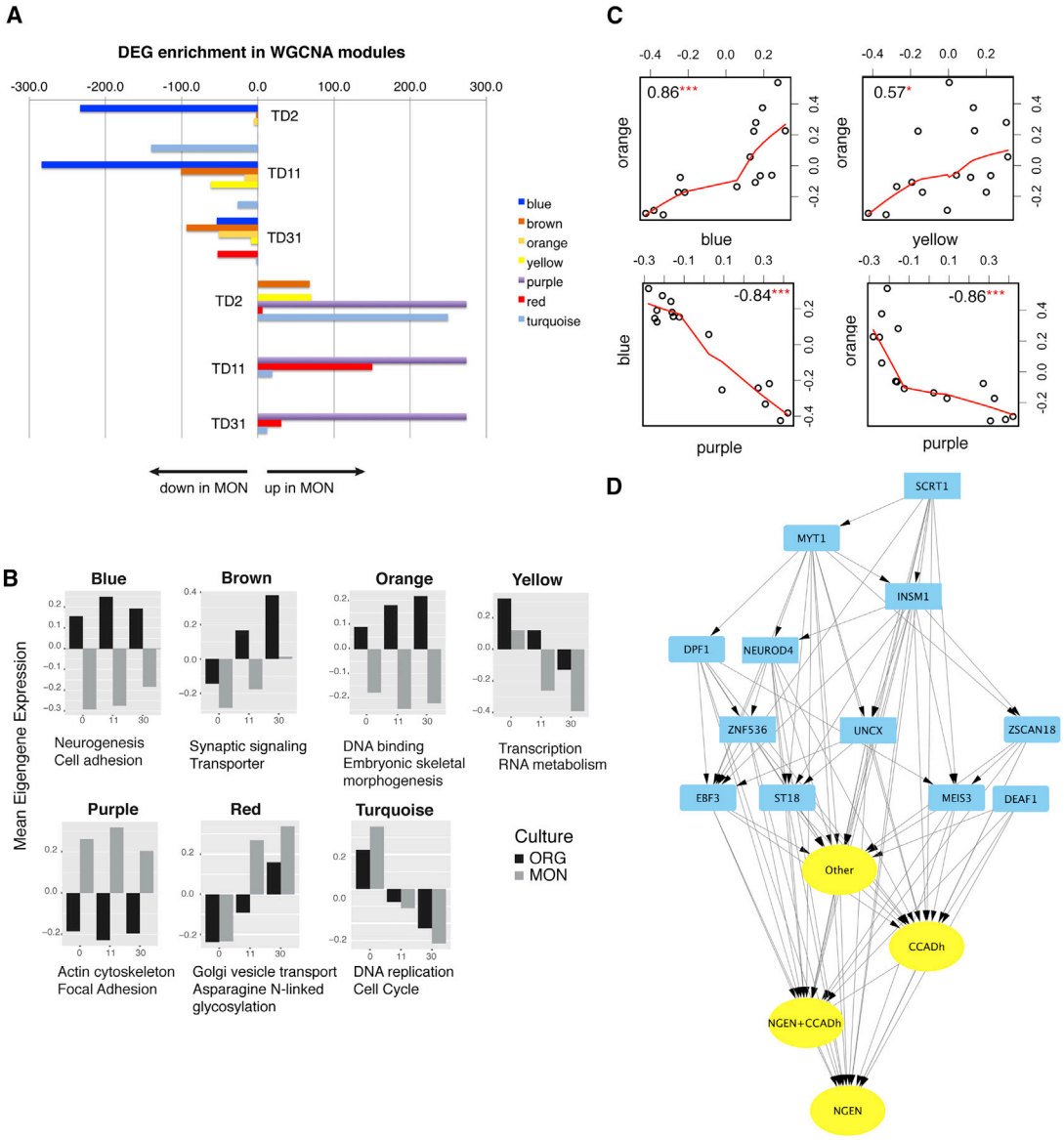

Figure 6. Characterization of the Seven Transcript Modules Differentially Expressed between MONs and ORGs

(A) Modules' overlap q values (as –log10 [q-value]) with DEGs in MONs versus ORGs at each time point.

(B) Barplots of modules' eigengenes versus time in MONs and ORGs. Reported also are the top scoring functional annotation for each module.

(C) Module to module correlation plots. Represented are the eigengenes as dots and the corresponding correlation coefficients.

(D) Blue module subnetwork, focusing on inferred TFs and associated target genes, as described in Table S7C, after filtering out any edge with an absolute value of the correlation coefficient <0.5. Yellow ovals, cell adhesion (CCADh)-related genes and neurogenesis (NGEN)-related genes, differentially expressed between MONs and ORGs that are TF targets. Blue, upstream TF; arrows, direction of TF-target relationship.

See also Figure S5 and Tables S6 and S7.

Dissociation-Induced Transcriptional Alterations Are Independent of Neural Induction Protocol

To assess the reproducibility of the observed dissociation-induced transcriptional alterations, we repeated the experiments using the same iPSC lines with a different neuronal induction protocol that uses the Dual-SMAD inhibition (Figure 7A). Similarly to our previous experiment, we generated ORGs, as well as parallel MONs and REAGs, after early dissociation at TD0, and used RNA-seq to infer transcriptional alterations in MONs

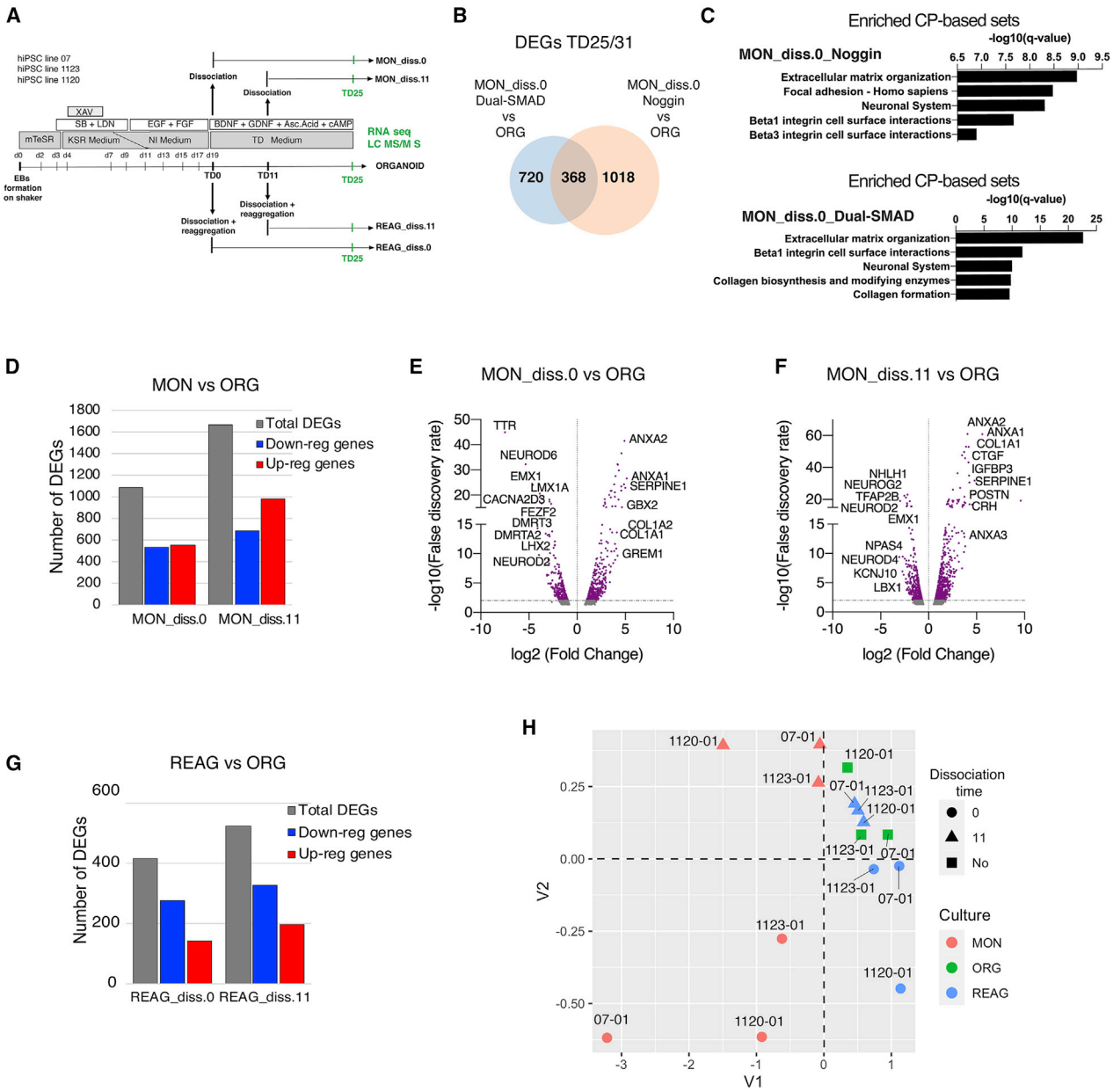

Figure 7. Consistency of Transcriptomic Changes between MONs and ORGs across Protocols and Times of Dissociation

(A) Experimental design. Cells derived from three iPSC lines were processed for transcriptomic or proteomic analysis. Abbreviations as in the text.

(B) Venn diagram showing overlap between early dissociated MON versus ORG DEGs under Noggin (n = 2 biological different iPSC lines per condition) or Dual-SMAD neuronal induction protocol (n = 3 biologically different iPSC lines per condition).

(C) Top CP-based annotations for the sets of DEGs between early dissociated MONs versus ORGs under Noggin and Dual-SMAD protocols, respectively.

(D) Total number of DEGs (gray bar), downregulated DEGs (blue bar), and upregulated DEGs (red bar) in early and late dissociated MONs versus ORGs at TD25.

(E and F) Volcano plots of MON_diss.0 versus ORG (E) and MON_diss.11 versus ORG (F) DEGs after early and late dissociation. Dots above the horizontal line are statistically significant (FDR < 0.01).

(G) Total number of DEGs (gray bar), downregulated DEGs (blue bar), and upregulated DEGs (red bar) in early and late REAGs versus ORGs at TD25.

(H) Multidimensional scaling plot of RNA-seq data at TD25 for all conditions.

and REAGs, compared with the intact ORGs, our reference preparation. The samples generated in this replication experiment, the DEGs between MONs and REAGs compared with ORGs, and their GO and CP annotations are listed in Tables S8A–S4D. We identified 1,088 DEGs in MONs versus ORGs, which we tested for overlap with the 1,386 previously identified DEGs under the Noggin protocol. We observed a significant overlap between the two lists of DEGs (368 genes, $p < 10^{-165}$) (Figure 7B), strong correlation in $\log_2$ fold change in gene expression (correlation coefficient ~0.76; not shown), and virtually identical top CP and GO terms for the sets of 1,088 and 1,386 DEGs comparing MONs versus ORGs under Noggin and Dual-SMAD protocols (Figure 7C), suggesting that dissociation-induced key transcriptional alterations are not specific to the Noggin protocol.

Time of Dissociation Has Marginal Effects on Transcriptional Alterations

To investigate whether there is a critical period when cell-to-cell contact must be maintained for proper forebrain neurogenesis, we generated MON and REAG cultures after a later dissociation time point at TD11 (respectively, MON_diss.11 and REAG_diss.11) along with those described previously after dissociation at TD0, using the Dual-SMAD inhibition protocol described above. We then compared DEGs between the early dissociated MONs versus ORGs (1,088) with the DEGs between the late dissociated MONs versus ORGs (1,667) (Figure 7D). We found nearly 500 DEGs in common, which also displayed good correlation in direction of change (correlation coefficient $r = 0.795$) (Figures S6A and S6B). Early and late dissociation DEGs sets showed overlap of CP and GO terms, specifically *Extracellular Matrix*-related terms for genes upregulated in MONs and *Nervous System Development* and *Neurogenesis* for genes upregulated in ORGs (Figures S6C–S6F; Tables S8A–S8D). Top upregulated genes in both early and late dissociated MON preparations included several collagen types (*COL1A1*, *COL1A2*) and gene products involved in ECM organization (*SERPINE1*, *CTGF*, *GREM1*, *ANXA1*, and *ANXA2*), and top downregulated genes included many neurogenic TFs (NEUROD2, EMX1/2) and deep and upper cortical layer neuronal markers (*BCL11B*, *FEZF2*, and *CUX2*) (Figures 7E, 7F, and S6G).

When gene expression in the REAG conditions was compared with the ORGs, early (REAG_diss.0) and late (REAG_diss.11) dissociation revealed only 417 and 523 DEGs (Figure 7G; Table S8A), respectively, confirming a weaker transcriptional perturbation compared with the MON condition, as described previously with the Noggin protocol (Figure 5B).

Indeed, multidimensional scaling showed a clear separation along the V1 axis between MON conditions and everything else (REAGs and ORGs), while along the V2 axis we observed a separation associated with the early versus late dissociation, more pronounced in MONs than in REAGs. Also, there was a wider spread in early dissociation versus late dissociation, more pronounced in REAGs, perhaps suggesting that late dissociation results in lower line-to-line variability, possibly because of a less drastic perturbation on the phenotype. In particular, the late dissociation REAGs seem closer to the ORGs, further supporting the idea that a later dissociation has less disruptive effect on neural development (Figure 7H).

Next, we used mass spectrometry-based label-free quantitative proteomics in two cell lines to interrogate proteome alterations between early dissociated MON and ORG conditions. We quantified 4,783 peptides across all conditions, with approximately 90% overlap with the list of expressed genes (Figure S6H). We then tested proteins for differential expression in MON_diss.0 versus ORG and identified 199 differentially expressed proteins (DEPs) (FDR < 0.05) with 107 upregulated (i.e., up in MONs) and 92 downregulated proteins (i.e., up in ORGs) (Figure S6I). The list of DEPs and their GO and CP annotations are presented in Tables S8E and S8F.

While comparison of the DEPs with the DEGs (Figure S6J), under identical conditions, resulted in modest overlap (about 30 DEPs also found as DEGs), this is consistent with previous work (Freiberg et al., 2016; Ghazalpour et al., 2011; Pacheco et al., 2017), and is likely related to the generally poor correlation between protein and transcript abundance (Haider and Pal, 2013; Vogel and Marcotte, 2012). Nevertheless, among the top GO terms associated to the upregulated proteins in MONs we find terms all related to focal adhesion and the cell-substrate adherens junction (Figure S6K). Among the top DEPs, also in overlap with the cell-substrate adhesion annotations, were gene products, such as FLNA/B, VCL, TLN1/2, ACTN1/4, PLEC, and ILK/Integrin linked kinase, linking the plasma cell membrane with the cortical actin cytoskeleton and interacting with integrins and other transmembrane receptors. Therefore, there is a consistent functional annotation between gene and proteins upregulated in MONs, both supporting a role of cell adhesion and ECM in disrupting cellular organization and fate. Interestingly, the DEPs offer a different, complementary picture with respect to the differential gene expression, providing insights into potential additional mechanisms that are impacted by variations in cell-to-cell contacts, e.g., the cell cytoskeleton, including contractile proteins, such as actin, myosin, and associated molecules, that influence cell shape as well as the symmetry of cell divisions, processes which may be highly disrupted by culture on a 2D substrate.

DISCUSSION

In this work, we compare the ability to generate cortical neural progenitor cells, and subsequently neurons, from three human iPSC lines differentiated under 3D ORG versus 2D MON conditions, using two different directed differentiation protocols. Longitudinal transcriptome analyses revealed that dissociation introduced a wave of transient transcriptional alterations dissipating over time, as the number of DEGs decrease from about a total of 8,500 to 8,000 at TD2 to 1,300 to 1,000 at TD31. However, the proportion of strong transcriptional alterations increased with time, delineating a picture of divergent systems with a more and more defined identity. Important signaling molecules and cell fate determinants were altered in the MONs at all time points analyzed, including a downregulation of cell-to-cell adhesion molecules, Notch pathway genes, and cortical cell fate genes, with a concomitant upregulation of cell-to-substrate adhesion molecules, including collagens, integrins, and laminins. Thus, contrasting MON with ORG transcriptomes over time and both preparations with fetal human brain (Figures 3H and 3I) does not support a maturational delay, i.e., a closer similarity of MONs to ORGs or to fetal brain at the later time point.

This is consistent with previous findings of divergent changes in cell membrane and ECM molecules when comparing 3D versus 2D differentiations (Simao et al., 2018). The potentially permanent result of this dynamic process may have led MONs onto a different developmental trajectory, at least within the observed temporal window.

Inhibiting ITGβ1 receptor signaling in MONs decreased cell-to-matrix adhesion and normalized cell division to levels comparable with ORGs, suggesting that increased ITG-laminin interactions are causing excessive proliferation. This is consistent with previous works showing that laminin promotes human primary neurosphere growth (Hall et al., 2008). However, suppressing ITGβ1 signaling in MONs did not change the downregulated expression of neurogenic and telencephalic cell fate genes. Thus, excessive ECM signaling causes abnormalities in cell proliferation but is not related to aberrant cell fate in this model.

A likely reason for the impaired differentiation of MONs is that loss of cell-to-cell contacts decreases intercellular signaling, while at the same time enhancing relatively unspecific cell-ECM contacts with laminin. In support of this, the prompt reaggregation of the dissociated neuronal progenitor cells partially restored aberrant cell fate. However, REAG preparations still displayed a disorganized architecture, with decreased RG cell polarity, smaller rosette structures, and loss of clear separation between RG and the postmitotic cell layer due to intermixing of newly born neurons with progenitor cells. Dissociation at a later time point did not substantially improve the differences in gene expression between MONs and ORGs, although transcriptomes of late dissociated REAGs were closer to those of ORGs. Overall, the data suggest that even a temporary disruption of cell-to-cell contacts, especially at early time points, has profound and possibly permanent effects.

Crucial components of layer- and compartment-specific cell adhesion are proto-cadherins and cadherin surface molecules. Cadherin-mediated junctions are located between the apical endfeet of RG cells and regulate mitotic spindle orientation, cortical architecture, and cell fate (Chilov et al., 2011; Gloerich et al., 2017; Tuncay and Ebnet, 2016). We show that, along with decreased CDH2 protein expression along their apical endfeet, the polarized organization of RG cells is almost completely lost in MONs and REAGs. Focused cell-to-cell Notch signaling and translocation of the Notch intracellular domain to RG nuclei promotes RG self-renewal (Hatakeyama et al., 2014). We indeed observed a global suppression in Notch signaling in MONs, including downstream proneural and neurogenic genes. This was likely the result of disruption in CDH2-containing apical complexes, as shown by the partial reversal of Notch and neurogenic gene expression upon reaggregation.

However, rather than premature differentiation, as often seen after disruption of apical complexes in animal models (Bultje et al., 2009; Cappello et al., 2006; Kim et al., 2010; Rousso et al., 2012; Zhang et al., 2010), we observed defective activation of proneural genes (i.e., *NEUROG1/2* and *NEUROD1/4/6*) and outer RG genes (e.g., *FAM*107A, *MT3*, and *HOPX*) in MONs compared with ORGs, suggesting an impaired capability of RG cells to give rise not only to other RG cells, but also to intermediate progenitors, outer RG progenitors, and early neurons. This could perhaps be attributed to a role of cell adhesion in controlling the spread and stability of Notch-dependent *HES1* and *DLL/NEUROG2* transcriptional oscillations between adjacent RG cells, oscillations which precede sustained *NEUROG2* expression, which is required for neuronal differentiation (Imayoshi et al., 2013; Shimojo et al., 2011). NEUROG2$^+$ progenitors, in turn, upregulate the transcriptional repressors *FOXP2/4*, *MYT1*, *INSM1*, and *SCRT1*, which downregulate *CDH2* transcription and promote detachment of TBR2$^+$ IPCs and outer RG from the ventricular layer (Itoh et al., 2013; Rousso et al., 2012; Tavano et al., 2018; Vasconcelos et al., 2016). This reciprocal regulation between RG cells and nascent neurons is maintained in the ORGs, as corroborated by co-expression of Notch-related genes, cadherins, and the above-mentioned IPC transcriptional repressors *MYT1*, *INSM1*, and *SCRT1* within the blue module, but fails to be implemented in the MONs where all these genes are downregulated. Owing to a lack of such cell-to-cell

contacts, MON and to a certain extent REAG preparations fail to reproducibly implement and maintain IPC generation and cortical neurogenesis.

Overall, the evidence supports a fundamental role of contacts between precursor cells in triggering and maintaining dynamic intercellular signaling systems, including cadherins and Notch, and undoubtedly others that govern the regional and cellular fate commitment of neuronal progenitors.

EXPERIMENTAL PROCEDURES

Neuronal Differentiation of iPSC Lines

We used three previously generated human male control iPSC lines (Mariani et al., 2015). Telencephalic ORGs were differentiated as described previously (Mariani et al., 2015). To generate MONs, neuronal rosettes were dissociated into single cells at TD0 and plated onto poly-L-ornithine- and laminin-coated wells, and, to generate REAGs, cell suspensions were quickly re-aggregated in a 96-well plate. The experiment was repeated using the same lines differentiated with a Dual-SMAD inhibition protocol adapted from Rigamonti et al. (2016) with SB431542 and LDN-193189 in place of Noggin (see the Supplemental Experimental Procedures and Table S1). Immunostaining, stereological analysis, qRT-PCR, and western blot analysis were performed as described in the Supplemental Experimental Procedures.

Transcriptomic and Proteomic Analysis

Samples (see Table S1) were processed for RNA-seq and label-free liquid chromatography-tandem mass spectrometry (LC-MS/MS) analysis as described in the Supplemental Experimental Procedures. RNA-seq reads were mapped to the human genome (hg19) and the GencodeV7 (Harrow et al., 2012) transcriptome annotation. DEGs were inferred using the edgeR pipeline, and an FDR cut-off of 0.05 was used for all the tests. We used the WGCNA package (Langfelder and Horvath, 2008) for co-expression network analysis using gene expression estimates (as log2 (RPKM + 1)) from all the iPSC-derived ORGs (three cell lines and three time points). We inferred TFs potentially upstream of genes within the blue module using the Enrichr web application (Kuleshov et al., 2016) and filtered out non-significant TFs (see the Supplemental Experimental Procedures). The LC-MS/MS data were processed using Proteome Discoverer (v.2.1; Thermo Fisher Scientific) and protein identification was carried out using the Mascot search algorithm (Matrix Science), and analyzed using Scaffold (Proteome Software).

Data and Code Availability

The source data described in this manuscript are available via the PsychENCODE Knowledge Portal (https://psychencode.synapse.org/). The PsychENCODE Knowledge Portal is a platform for accessing data, analyses, and tools generated through grants funded by the National Institute of Mental Health (NIMH) PsychENCODE program. The accession number for RNA-seq and proteomic data reported in this paper is https://doi.org/10.7303/syn23593358. Data are available for general research use after complying with requirements for data access and data attribution.

SUPPLEMENTAL INFORMATION

Supplemental Information can be found online at https://doi.org/10.1016/j.stemcr.2020.12.019.

AUTHOR CONTRIBUTIONS

F.M.V. and G.C. conceived the study. F.M.V. supervised the project. G.G.A., S.S., and G.C. designed, performed, and analyzed experiments. G.C. analyzed RNA-seq and LC-MS/MS data. F.M.V., S.S., and G.C. prepared display items. G.G.A., S.S., G.C., and F.M.V. wrote the manuscript. All authors participated in discussion of results and manuscript editing.

ACKNOWLEDGMENTS

We thank Junhyun Park for his help in stereological analyses, Kaya Bilguvar and Christopher Castaldi of the Yale Center for Genomic Analysis for help with RNA sequencing and Rashaun Wilson and TuKiet T. Lam of the W.M. Keck Foundation Biotechnology Resource Laboratory at Yale University for help with the LC-MS/MS. We thank Jessica Mariani, Anahita Amiri, and Alexandre Jourdon for help with the neuronal Dual-SMAD protocol, and Jeremy Schreiner for proofreading and editing the manuscript.

This work was funded by NIH grants U01 MH103365 and R01 MH109648, and by the Harris Family Professorship fund. We are grateful to the Sage Bionetworks Data Coordination Center for help with data access.

Received: July 14, 2019
Revised: December 29, 2020
Accepted: December 31, 2020
Published: January 28, 2021

REFERENCES

Ardhanareeswaran, K., Mariani, J., Coppola, G., Abyzov, A., and Vaccarino, F.M. (2017). Human induced pluripotent stem cells for modelling neurodevelopmental disorders. Nat. Rev. Neurol. *13*, 265–278.

Arlotta, P., and Pasca, S.P. (2019). Cell diversity in the human cerebral cortex: from the embryo to brain organoids. Curr. Opin. Neurobiol. *56*, 194–198.

Bultje, R.S., Castaneda-Castellanos, D.R., Jan, L.Y., Jan, Y.N., Kriegstein, A.R., and Shi, S.H. (2009). Mammalian Par3 regulates progenitor cell asymmetric division via notch signaling in the developing neocortex. Neuron *63*, 189–202.

Camp, J.G., Badsha, F., Florio, M., Kanton, S., Gerber, T., Wilsch-Brauninger, M., Lewitus, E., Sykes, A., Hevers, W., Lancaster, M., et al. (2015). Human cerebral organoids recapitulate gene expression programs of fetal neocortex development. Proc. Natl. Acad. Sci. U S A *112*, 15672–15677.

Cappello, S., Attardo, A., Wu, X., Iwasato, T., Itohara, S., Wilsch-Brauninger, M., Eilken, H.M., Rieger, M.A., Schroeder, T.T.,

Huttner, W.B., et al. (2006). The Rho-GTPase cdc42 regulates neural progenitor fate at the apical surface. Nat. Neurosci. *9*, 1099–1107.

Chambers, S.M., Fasano, C.A., Papapetrou, E.P., Tomishima, M., Sadelain, M., and Studer, L. (2009). Highly efficient neural conversion of human ES and iPS cells by dual inhibition of SMAD signaling. Nat. Biotechnol. *27*, 275–280.

Chilov, D., Sinjushina, N., Rita, H., Taketo, M.M., Makela, T.P., and Partanen, J. (2011). Phosphorylated beta-catenin localizes to centrosomes of neuronal progenitors and is required for cell polarity and neurogenesis in developing midbrain. Dev. Biol. *357*, 259–268.

Eiraku, M., Watanabe, K., Matsuo-Takasaki, M., Kawada, M., Yonemura, S., Matsumura, M., Wataya, T., Nishiyama, A., Muguruma, K., and Sasai, Y. (2008). Self-organized formation of polarized cortical tissues from ESCs and its active manipulation by extrinsic signals. Cell Stem Cell *3*, 519–532.

Engler, A.J., Sen, S., Sweeney, H.L., and Discher, D.E. (2006). Matrix elasticity directs stem cell lineage specification. Cell *126*, 677–689.

Freiberg, J.A., Le Breton, Y., Tran, B.Q., Scott, A.J., Harro, J.M., Ernst, R.K., Goo, Y.A., Mongodin, E.F., Goodlett, D.R., McIver, K.S., et al. (2016). Global analysis and comparison of the transcriptomes and proteomes of group A *Streptococcus* biofilms. mSystems *1*, e00149-16.

Ghazalpour, A., Bennett, B., Petyuk, V.A., Orozco, L., Hagopian, R., Mungrue, I.N., Farber, C.R., Sinsheimer, J., Kang, H.M., Furlotte, N., et al. (2011). Comparative analysis of proteome and transcriptome variation in mouse. PLoS Genet. *7*, e1001393.

Gloerich, M., Bianchini, J.M., Siemers, K.A., Cohen, D.J., and Nelson, W.J. (2017). Cell division orientation is coupled to cell-cell adhesion by the E-cadherin/LGN complex. Nat. Commun. *8*, 13996.

Haider, S., and Pal, R. (2013). Integrated analysis of transcriptomic and proteomic data. Curr. Genomics *14*, 91–110.

Hall, P.E., Lathia, J.D., Caldwell, M.A., and Ffrench-Constant, C. (2008). Laminin enhances the growth of human neural stem cells in defined culture media. BMC Neurosci. *9*, 71.

Harrow, J., Frankish, A., Gonzalez, J.M., Tapanari, E., Diekhans, M., Kokocinski, F., Aken, B.L., Barrell, D., Zadissa, A., Searle, S., et al. (2012). GENCODE: the reference human genome annotation for the ENCODE Project. Genome Res. *22*, 1760–1774.

Hatakeyama, J., Wakamatsu, Y., Nagafuchi, A., Kageyama, R., Shigemoto, R., and Shimamura, K. (2014). Cadherin-based adhesions in the apical endfoot are required for active Notch signaling to control neurogenesis in vertebrates. Development *141*, 1671–1682.

Iba, K., Albrechtsen, R., Gilpin, B., Frohlich, C., Loechel, F., Zolkiewska, A., Ishiguro, K., Kojima, T., Liu, W., Langford, J.K., et al. (2000). The cysteine-rich domain of human ADAM 12 supports cell adhesion through syndecans and triggers signaling events that lead to beta1 integrin-dependent cell spreading. J. Cell Biol. *149*, 1143–1156.

Imayoshi, I., Isomura, A., Harima, Y., Kawaguchi, K., Kori, H., Miyachi, H., Fujiwara, T., Ishidate, F., and Kageyama, R. (2013). Oscillatory control of factors determining multipotency and fate in mouse neural progenitors. Science *342*, 1203–1208.

Itoh, Y., Moriyama, Y., Hasegawa, T., Endo, T.A., Toyoda, T., and Gotoh, Y. (2013). Scratch regulates neuronal migration onset via an epithelial-mesenchymal transition-like mechanism. Nat. Neurosci. *16*, 416–425.

Johnson, M.B., Wang, P.P., Atabay, K.D., Murphy, E.A., Doan, R.N., Hecht, J.L., and Walsh, C.A. (2015). Single-cell analysis reveals transcriptional heterogeneity of neural progenitors in human cortex. Nat. Neurosci. *18*, 637–646.

Kim, S., Lehtinen, M.K., Sessa, A., Zappaterra, M.W., Cho, S.H., Gonzalez, D., Boggan, B., Austin, C.A., Wijnholds, J., Gambello, M.J., et al. (2010). The apical complex couples cell fate and cell survival to cerebral cortical development. Neuron *66*, 69–84.

Kuleshov, M.V., Jones, M.R., Rouillard, A.D., Fernandez, N.F., Duan, Q., Wang, Z., Koplev, S., Jenkins, S.L., Jagodnik, K.M., Lachmann, A., et al. (2016). Enrichr: a comprehensive gene set enrichment analysis web server 2016 update. Nucleic Acids Res. *44*, W90–W97.

Lancaster, M.A., Renner, M., Martin, C.A., Wenzel, D., Bicknell, L.S., Hurles, M.E., Homfray, T., Penninger, J.M., Jackson, A.P., and Knoblich, J.A. (2013). Cerebral organoids model human brain development and microcephaly. Nature *501*, 373–379.

Langfelder, P., and Horvath, S. (2008). WGCNA: an R package for weighted correlation network analysis. BMC Bioinformatics *9*, 559.

Long, K., Moss, L., Laursen, L., Boulter, L., and ffrench-Constant, C. (2016). Integrin signalling regulates the expansion of neuroepithelial progenitors and neurogenesis via Wnt7a and Decorin. Nat. Commun. *7*, 10354.

Mariani, J., Coppola, G., Zhang, P., Abyzov, A., Provini, L., Tomasini, L., Amenduni, M., Szekely, A., Palejev, D., Wilson, M., et al. (2015). FOXG1-dependent dysregulation of GABA/glutamate neuron differentiation in autism spectrum disorders. Cell *162*, 375–390.

Mariani, J., Simonini, M.V., Palejev, D., Tomasini, L., Coppola, G., Szekely, A.M., Horvath, T.L., and Vaccarino, F.M. (2012). Modeling human cortical development in vitro using induced pluripotent stem cells. Proc. Natl. Acad. Sci. U S A *109*, 12770–12775.

Milner, R., and Campbell, I.L. (2002). The integrin family of cell adhesion molecules has multiple functions within the CNS. J. Neurosci. Res. *69*, 286–291.

Nowakowski, T.J., Bhaduri, A., Pollen, A.A., Alvarado, B., Mostajo-Radji, M.A., Di Lullo, E., Haeussler, M., Sandoval-Espinosa, C., Liu, S.J., Velmeshev, D., et al. (2017). Spatiotemporal gene expression trajectories reveal developmental hierarchies of the human cortex. Science *358*, 1318–1323.

Pacheco, N.L., Heaven, M.R., Holt, L.M., Crossman, D.K., Boggio, K.J., Shaffer, S.A., Flint, D.L., and Olsen, M.L. (2017). RNA sequencing and proteomics approaches reveal novel deficits in the cortex of Mecp2-deficient mice, a model for Rett syndrome. Mol. Autism *8*, 56.

Pollen, A.A., Nowakowski, T.J., Chen, J., Retallack, H., Sandoval-Espinosa, C., Nicholas, C.R., Shuga, J., Liu, S.J., Oldham, M.C., Diaz, A., et al. (2015). Molecular identity of human outer radial glia during cortical development. Cell *163*, 55–67.

Rigamonti, A., Repetti, G.G., Sun, C., Price, F.D., Reny, D.C., Rapino, F., Weisinger, K., Benkler, C., Peterson, Q.P., Davidow, L.S., et al. (2016). Large-scale production of mature neurons from human pluripotent stem cells in a three-dimensional suspension culture system. Stem Cell Reports *6*, 993–1008.

Rousso, D.L., Pearson, C.A., Gaber, Z.B., Miquelajauregui, A., Li, S., Portera-Cailliau, C., Morrisey, E.E., and Novitch, B.G. (2012). Foxp-mediated suppression of N-cadherin regulates neuroepithelial character and progenitor maintenance in the CNS. Neuron *74*, 314–330.

Saha, K., Keung, A.J., Irwin, E.F., Li, Y., Little, L., Schaffer, D.V., and Healy, K.E. (2008). Substrate modulus directs neural stem cell behavior. Biophys. J. *95*, 4426–4438.

Shi, Y., Kirwan, P., Smith, J., Robinson, H.P., and Livesey, F.J. (2012). Human cerebral cortex development from pluripotent stem cells to functional excitatory synapses. Nat. Neurosci. *15*, 477–486.

Shimojo, H., Ohtsuka, T., and Kageyama, R. (2011). Dynamic expression of notch signaling genes in neural stem/progenitor cells. Front. Neurosci. *5*, 78.

Sidhaye, J., and Knoblich, J.A. (2021). Brain organoids: an ensemble of bioassays to investigate human neurodevelopment and disease. Cell Death Differ. *28*, 52–67.

Simao, D., Silva, M.M., Terrasso, A.P., Arez, F., Sousa, M.F.Q., Mehrjardi, N.Z., Saric, T., Gomes-Alves, P., Raimundo, N., Alves, P.M., et al. (2018). Recapitulation of human neural microenvironment signatures in iPSC-derived NPC 3D differentiation. Stem Cell Reports *11*, 552–564.

Takahashi, K., Tanabe, K., Ohnuki, M., Narita, M., Ichisaka, T., Tomoda, K., and Yamanaka, S. (2007). Induction of pluripotent stem cells from adult human fibroblasts by defined factors. Cell *131*, 861–872.

Tavano, S., Taverna, E., Kalebic, N., Haffner, C., Namba, T., Dahl, A., Wilsch-Brauninger, M., Paridaen, J., and Huttner, W.B. (2018). Insm1 induces neural progenitor delamination in developing neocortex via downregulation of the adherens junction belt-specific protein Plekha7. Neuron *97*, 1299–1314.e8.

Tuncay, H., and Ebnet, K. (2016). Cell adhesion molecule control of planar spindle orientation. Cell. Mol. Life Sci. *73*, 1195–1207.

Vasconcelos, F.F., Sessa, A., Laranjeira, C., Raposo, A., Teixeira, V., Hagey, D.W., Tomaz, D.M., Muhr, J., Broccoli, V., and Castro, D.S. (2016). MyT1 counteracts the neural progenitor program to promote vertebrate neurogenesis. Cell Rep. *17*, 469–483.

Vogel, C., and Marcotte, E.M. (2012). Insights into the regulation of protein abundance from proteomic and transcriptomic analyses. Nat. Rev. Genet. *13*, 227–232.

Yu, J., Vodyanik, M.A., Smuga-Otto, K., Antosiewicz-Bourget, J., Frane, J.L., Tian, S., Nie, J., Jonsdottir, G.A., Ruotti, V., Stewart, R., et al. (2007). Induced pluripotent stem cell lines derived from human somatic cells. Science *318*, 1917–1920.

Zhang, J., Woodhead, G.J., Swaminathan, S.K., Noles, S.R., McQuinn, E.R., Pisarek, A.J., Stocker, A.M., Mutch, C.A., Funatsu, N., and Chenn, A. (2010). Cortical neural precursors inhibit their own differentiation via N-cadherin maintenance of beta-catenin signaling. Dev. Cell *18*, 472–479.

Stem Cell Reports, Volume *16*

Supplemental Information

Cell-to-Cell Adhesion and Neurogenesis in Human Cortical Development: A Study Comparing 2D Monolayers with 3D Organoid Cultures

Soraya Scuderi, Giovanna G. Altobelli, Vincenzo Cimini, Gianfilippo Coppola, and Flora M. Vaccarino

Cell-to-cell adhesion and neurogenesis in human cortical development: a study comparing 2D monolayers with 3D organoid cultures

Soraya Scuderi[1,5], Giovanna G. Altobelli[1,2,5], Vincenzo Cimini[2], Gianfilippo Coppola[1,4,*], Flora M. Vaccarino[1,3,*]

Supplemental Experimental Procedures

Neuronal Differentiation of hiPSC lines. Noggin protocol. We differentiated three human male control iPSC cell lines (07-01#1, 1123-01#3, 1120-01#7) into telencephalic neurons according to our established method (Mariani et al., 2015). Human iPS cells were dissociated to single cells with Accutase (Chemicon), and a total of 3.2 million cells was plated in AggreWell™ 800 plates and cultured in DMEM/F12-GLUTAMAX (neuronal medium) with 4% B27 without vitamin A, 1% N2 and supplemented with recombinant mouse Noggin (R&D Systems 1967-NG-025) and Y-27632. After 2 days, embryoid bodies (EBs) were collected and plated onto 10-cm bacterial Petri dishes in neuronal medium as above with the addition of B27 supplemented with vitamin A**,** Y-27632 and Noggin. On Day 4, free-floating EBs were collected and plated in neuronal medium, supplemented with only Noggin, onto 10 cm tissue culture dishes coated with growth factor-reduced Matrigel (BD Bioscience, diluted 1:30 with DMEM:F12 medium) to allow neural rosette formation. The next day (day 5), the neuronal medium was changed and supplemented with 20 ng/ml FGF2, 200 ng/ml Noggin, and 200 ng/ml rhDkk1 (R&D Systems, 5439-DK). After two or three days the neural rosettes were manually dissected and replated as free-floating aggregates in 10-cm bacterial Petri dishes in neuronal medium supplemented with FGF2 (10 ng/ml) and EGF (10 ng/ml). For the dissociation followed by immediate re-aggregation (REAG) and monolayer (MON) culture conditions, after 4 days in suspension, neuronal rosettes were dissociated to single cells with Accutase and quickly re-aggregated (20,000 cells) in a low cell adhesion 96 well plate (REAG), or plated (30,000 cells/0.8cm^2) onto poly-L-ornithine and laminin coated 8 well permanox chamber slides (Thermo Scientific) as adherent monolayer cultures (MON). Alternatively, for the organoid (ORG) condition, free-floating aggregates were left undissociated (see **Figure 1A**). All preparations were kept in the same neuronal medium supplemented with FGF2 and EGF for another day. The next day all preparations were transferred in growth factor-free neurobasal-type medium supplemented with BDNF (R&D), GDNF (R&D), ascorbic acid, and dibutyryl-cAMP (Sigma). This medium change triggers the onset of terminal differentiation (TD) and thus, this day is indicated TD day 0 (TD 0). **Dual SMAD inhibition protocol.** The same three iPSC lines were differentiated into cortical neurons by using a modified version of the Dual-SMAD neuronal induction protocol of Rigamonti et al.,2016 (Rigamonti et al., 2016), that use SB431542 and LDN-193189 in place of Noggin. Media used were: *mTeSR™ Plus* (STEMCELL Technologies, #100-0276); *KSR medium*: 15% KSR (Invitrogen), KO DMEM (Invitrogen), L-glutamine (Gibco), 100X non-essential amino acids (NEAA) (Gibco), 100X penicillin-streptomycin (Gibco), and 1000X b-mercaptoethanol (Gibco); *Neural induction medium* (NIM): DMEM/F12 (Invitrogen), 100X N2 supplement (Gibco), 50X B27 supplement without vitamin A (Life Technologies),100X Glutamax (Gibco), 100X NEAA (Gibco), 100X penicillin-streptomycin (Gibco), 0.15% D-(+)-Glucose solution (Sigma G8644). Human iPSCs were dissociated by Accutase into a single cells suspension (day 0), and a total of 4 million cells was plated into a well of 6-multiwell plate and rotated on an orbital shaker (Labstrong) at 95 RPKM in mTeSR™ Plus medium with Y-27632 (5 μM) in a 37°C, 5% CO2. On day 2, the medium was replaced with fresh mTeSR™ Plus medium. At day 3 of differentiation, medium was changed to mTeSR with SB431542 (R&D Systems,10 mM) and LDN193189 (Stemgent,1 mM) (referred as Dual-SMAD inhibition). From day 4 to day 11 EBs were gradually adapted to neuronal induction medium (NIM) through a dilution series of KSR and NIM in the presence of Dual-SMAD inhibition throughout. Medium was changed as follows: day 4: 100% KSR medium with Wnt signaling inhibitor XAV939 (2 mM) (Stemgent); day 7: 75% KSR medium, 25% NIM; day 9: 50% KSR medium, 50% NIM; day 11: 25% KSR medium, 75% NIM. From days 13 to 18, cultures were maintained in 100% NIM supplemented with FGF2 (10 ng/ml) and EGF (10 ng/ml). From day 19 onward, cultures were maintained in neurobasal medium neurobasal-type medium supplemented with BDNF (R&D), GDNF (R&D), ascorbic acid, and dibutyryl-cAMP (Sigma). This medium change triggers the onset of terminal differentiation (TD) and thus, this day is indicated TD day 0 (TD 0). Re-aggregated culture (REAG) and monolayer (MON) conditions were generated in the same way as described above with the Noggin protocol at day 19 (TD0) where neuronal progenitor cells in EBs have organized themselves in rosettes structures evident at the brightfield microscope.

To examine the role of laminin/β1-ITG signaling, rosettes (obtained from hiPSC line 1123-01#3) were dissociated and plated as monolayer on Poly-l-ornithine/laminin, as described before, and grown for 2 (TD2) or 11 days (TD11),

with the addition of either 2μg/ml of IgG2bk Functional Grade Isotype Control (Thermo Fisher cat number 16-4732-85) or 2μg/ml of monoclonal antibody IgG2bk anti-human β1integrin (MilliporeSigma, MAB1959Z).

Immunofluorescence and stereological analysis. Organoids and reaggregates were fixed in 4% PFA for 3 hours, washed three times in PBS1X and transferred in 30% sucrose overnight at 4ºC, then embedded in OCT and cryosectioned at 14 μm. Monolayers were fixed in 4% PFA for 3 hours and washed three times in PBS1X. Cryosections or monolayers culture wells were blocked in 10% normal donkey serum (NDS)/0.1% Triton X-100/PBS for 1 hour at room temperature and incubated overnight at 4ºC with primary antibody diluted in a solution containing 5% NDS/0.05% Triton X-100/PBS. Sections were washed in PBS/0.1% Triton X-100 3 times and incubated for 1 hour with a secondary antibody diluted in 5% NDS/0.05% Triton X-100/PBS. Primary antibodies were as follows: goat anti-Sox1 (1:20; R&D Systems, AF 3369), mouse anti-Pax6 (1:200; BD Biosciences, 561462), mouse anti TUBB3 (1:1000; Promega, G712A), rabbit anti-Ki67 (1:500; Vector, VP-RM04), rabbit anti Tbr1 (1:1000; Abcam, ab31940), rat anti Citp2 (1:500; Abcam, 18465), rabbit anti GABA (1:500; Millipore, A2052), mouse anti GAD1/GAD67 (1:1000; Millipore, MAB5406), rat anti CTIP2/BCL11B (1:500; Abcam, ab18465), mouse anti β-Catenin (1:100; BD Transduction Laboratories, 610153), mouse anti-N-Cadherin (1:500; BD Transduction Laboratories, 610920). Nuclei were stained with DAPI. All images were acquired using an ApoTome-equipped Axiovert 200M with Axiovision 4.5 software. Quantification of immunostained cells was performed by stereological analysis using a Carl Zeiss Axioskop 2 Mot Plus, connected to a computer running Stereoinvestigator Software (MicroBrigh-Field) as previously described (Mariani et al., 2015).

Western Blot analysis. Western blot analysis was performed to determine protein expression levels as previously described (Scuderi et al., 2013). Samples were suspended in RIPA cell lysis buffer (Millipore 20-188) supplemented with Protease and Phosphatase inhibitor cocktail (Roche Diagnostics) and homogenized by using a teflon-glass homogenizer, then sonicated twice for 20 sec using an ultrasonic probe, followed by centrifugation at 10,000 g for 20 min at 4 °C. Protein concentration was determined by the Qubit Protein Assay Kit (Invitrogen). Samples (30 μg each) were diluted in 2X Laemmli buffer (Invitrogen, Carlsbad, CA, USA), denatured at 70°C for 10 min and proteins were separated on a Biorad Criterion XT 4-15% Bis-tris gel (BIO-RAD) by electrophoresis and then transferred to a nitrocellulose membrane (BIO-RAD). Blots were blocked using 5% bovine serum in Tris-buffered saline with 0.1% Tween 20 and probed with the following antibodies: 1:500 rabbit anti-TBR1 (cat n. 31940, Abcam), 1:500 rabbit anti-DCX antibody (cat n. 18723, Abcam), 1:200 goat anti-Neurogenin2 (cat n. SC19233, Santa Cruz Biotechnology), 1:500 mouse anti-GAPDH (cat n. MAB374 Millipore), 1:1000 rabbit anit-FAK (cat n. #3285, Cell Signaling), 1:1000 rabbit anti-Phospho-FAK(cat n. #8556, Cell Signaling). An anti-rabbit IgG HRP-linked antibody (cat #7074; Cell Signaling) or an anti-mouse IgG HRP-linked Antibody (cat #7076; Cell Signaling) or anti-goat IgG HRP-linked Antibody (cat n. 705-035-003 Jackson ImmunoResearch) were used. Blots were visualized using SuperSignal West Pico Chemioluminescent Substrate (Thermo Scientific, 34080), gels were quantified by using ImageJ (NIH) (Schindelin et al., 2012).

RNA isolation and RNA sequencing experiments. Total cellular RNA was collected from intact organoids and reaggregates (about 15-20 organoids for each line), and from two 9 cm^2 wells of a 6 wells plate for a monolayer culture at TD 2, TD 11 and TD 31 and purified using PicoPure RNA isolation kit (Applied Biosciences) as per manifacturer's instructions. Poly(A)+ RNA from 3 biologically different iPSC lines per condition (ORG, REAG and MON) was used as template for the preparation of 27 human cDNA libraries, which were then subject to single end RNA seq.

Quantitative real time RT-PCR. An aliquot of the Poly(A)+RNA from ORG, REAG and MON that was previously used for RNAseq analysis, was used for secondary validation through real-time PCR analysis. Our analysis revealed a correlation coefficient of 0.77 between log2 (fold changes) in expression from the two techniques. 10 ng of RNA was used for cDNA synthesis using SuperScript III First-strand synthesis Supermix and random hexamers (Invitrogen, #1808-051). Primers for 34 randomly picked differentially expressed genes were designed using NCBI/Primer-BLAST (**Table S3e**). PCR reactions were conducted on a StepOnePlus Real-Time PCR System (Applied Biosystems) by using a SYBR-green based method (Fast SYBR Green Master Mix, ABI) followed by melt curve analysis to verify specificity of the product. The Ct value was used to calculate the relative amount of mRNA molecules. The Ct value of each target gene was normalized by subtraction of the Ct value from GAPDH housekeeping genes to obtain the ΔCt value.

Statistical Analysis. Statistical analysis of cell counts, qPCR and Western blot assays was performed using GraphPad Prism Version 7 (GraphPad Software, USA). Significance was determined by Student t-test or ANOVA as indicated in figure legends. Results are expressed as mean ± SEM.

RNAseq data analysis. Sequencing reads were mapped to the human genome (hg19) and the GencodeV7 (Harrow et al., 2012) transcriptome annotation. The BEDtools function coverageBed (Quinlan and Hall, 2010) was used to estimate gene expression as counts. The R package edgeR (Robinson et al., 2010) was used to estimate gene expression as RPKM.

Differential expression analysis. Differentially expressed genes were inferred using the edgeR pipeline (Robinson et al., 2010), using the trended dispersion to estimate the biological variance. In one instance, where blocking by line would result in an N=1, we blocked by batch to have N=2 (see **Table S1a**). We contrasted cell culture models (i.e. MON vs ORG) and developmental time points (i.e. TD11 vs TD2 and TD31 vs TD11). Within each contrast, counts data were first filtered, by requiring that at least 50% plus one of the samples have a level of expression of 1 count per million or more. About 17000-20000 genes survived the filter and were further processed. Nominal p-values from differential expression analysis were FDR corrected, and an FDR cut-off of 0.05 was used for all the tests. Functional enrichment analysis. ConsensusPathDB (Kamburov et al., 2011) was used to test differentially expressed genes for overrepresentation in Gene Ontologies and Canonical Pathways.

Weighted gene co-expression network analysis. We used Weighted Gene Co-expression Network Analysis (WGCNA) (Langfelder and Horvath, 2008) for co-expression network analysis using gene expression estimates (as log2(RPKM+1)) from all the hiPSCs derived organoids (3 cell lines and 3 time points). We then estimated the co-expression network and modules using the function blockwiseModule with the following parameters: maxBlockSize=30000; corType=bicorr; power=30; networkType=signed; deepSplit=2; minModuleSize=50.
The analysis produced a network of 42 modules, corresponding to about 20214 genes, including the grey module of unassigned genes (**Table S6**). We used permutation analysis to verify that the modules identified were not artifacts of the clustering procedure. We assumed the mean topological overlap of a network module to be greater than the mean topological overlap of a random set of genes, in order for the module genes to be co-expressed beyond chance. For each module we estimated the average topological overlap (Langfelder and Horvath, 2008), then randomly selected a number of genes equal to the number of module members and estimated the corresponding mean topological overlap. This operation was repeated 100 times. The p-value for the analysis was estimated by dividing the number of times the mean topological overlap of the random set of genes was greater than that of the network module, by the number of permutations (N=100). Finally, the p-values for all the modules were FDR corrected for multiple comparisons, and a cut-off of 0.05 was considered for significance. All the modules passed the test and were considered for further analysis. Correlation analysis of modules' eigengenes was used to highlight module to module relationship (**Table S6**). We used ConsensusPathDB (Kamburov et al., 2011) for functional annotation of modules.

Transcription factor analysis. We inferred transcription factors (TFs) potentially upstream of genes within the blue module using the EnrichR online database (Kuleshov et al., 2016) and retained only statistically significant TFs at a fdr corrected p-value of 0.05. We then filtered out TFs whose target genes do not show overlap with the MON vs ORG DEGs list at all time points. This ensures that inferred TFs with no clear sign of activity are removed from downstream analysis. Next, we downloaded the Neurogenesis and the GO_CELL_CELL_ADHESION gene sets from the Broad Institute MSigDB (v6.2) collection (Liberzon et al., 2011; Subramanian et al., 2005). Then, we tested each TF-target for statistical overlap with the Neurogenesis gene set, and the resulting set was then tested for overlap with the cell-cell adhesion gene set. We retained only TFs showing overlap with both gene set at an FDR<0.05. We integrated the TF-target genes directed relationships derived from literature, with our undirected WGCNA network edges. This resulted in a directed network, with data driven edges strength (i.e. correlation coefficient), where non relevant edges (i.e. edges with zero correlation coefficients) could be filtered out. The resulting directed network highlights the regulatory relationship between the TFs that are upstream from the blue module and their target genes. Next, we estimated a weighted connectivity within this network, ranked the TFs in order of decreasing weighted connectivity. The resulting directed network highlights the regulatory relationship between the TFs that are upstream from the blue module and their target genes (**see Figure 6D**).

Creation of the neurodevelopmental genes list. We manually curated a neurodevelopmental list of genes by selecting group of genes whose function and expression has been previously described in published data from human

cortical developmental studies (Amiri et al., 2018; de la Torre-Ubieta et al., 2018; Hu et al., 2017; Johnson et al., 2015; Kang et al., 2011; Nowakowski et al., 2017; Pollen et al., 2014; Thomsen et al., 2016) and based on their annotation in existing datasets (KEGG pathway, HUGO Gene Nomenclature Committee). The neurodevelopmental genes list (**Table S4**) consists of the sublist Neuronal cell fate genes (168 genes), Cell Adhesion Molecules (247 genes) Axon Guidance (175 genes) and Extracellular Matrix (86 genes). We use this curated gene list to characterize the biological processes underlying the differences in gene expression among the ORG, MON and REAG conditions. For each comparison (e.g. MON vs ORG, REAG vs ORG) at each time point analyzed (TD2, TD11 TD 31), the log2(FC) of a DEGs of a specific category (sublists in **Table S4**) were collected into a data matrix, where each row represented one gene and each column represents one time point. After the matrix was created, a heat map plot was created by using GraphPadPrism Version 7 (GraphPad Software, USA).
We also interrogated a Dorsal-ventral forebrain Human Gene list obtained from the Human BRAINSPAN Developmental transcriptome (http://www.brainspan.org/rnaseq/search/index.html) by using differential search of target vs contrast structure and selecting human dorsolateral prefrontal cortex (DFC) vs basal telencephalon (e.g. lateral ganglionic eminence (LGE), medial ganglionic eminence (MGE), caudal ganglionic eminence (CGE), Striatum (STR)) and viceversa to obtain lists of up- or down-regulated genes in cortex and ventral telencephalon, respectively. The developmental stages selected were 8-9PCW, 10-12PCW and 13-15PCW, considering that ORG, the reference condition, best matches these human brain developmental stages (Amiri et al., 2018).

Mass Spectrometry (LC MS/MS)

Human iPSC derived neurons frozen cell pellets from ORG and MON at TD25 (2 iPSC lines, 07-01 and 1120), were lysed with RIPA buffer containing a protease and phosphatase inhibitor cocktail and with ultra-sonication (10% Amplitude, with 15 sec followed by 1 sec burst twice). Cellular debris were removed after centrifugation at 14,600g for 10 minutes at 4°Celsius. 100 µL of the supernatant was transferred to a new tube and proteins were precipitated with Chloroform:MeOH:water (100:400:300 µL). Protein pellets were washed three times with cold methanol prior to air drying for 5 minutes, and stored at -80°C. Dried protein pellets were resolubilized with 8M urea containing 400mM ammonium bicarbonate, reduced with dithiothreitol (DTT) at 37°C for 30 minutes, alkylated with iodoacetamide (IAN) at room temperature for 30 minutes in the dark, and then trypsin (1:50 enzyme:protein) digested twice, at 37°C overnight and at 37°C for 4 hours. Digestion was quenched with 20% trifluoroacetic acid, desalted using C18 reverse phase macrospin columns (The Nest Group Inc., Southborough, MA), and eluted peptides were dried using SpeedVac. Total peptides amount was determined by nanodrop (Thermo Fisher Scientific; Waltham, MA) High resolution tandem mass spectrometry was carried out on a Thermo Fisher Scientific Q-Exactive Plus connected to a UPLC system (Waters nanoACQUITY) equipped with a Waters Symmetry® C18 180 µm × 20 mm trap column and a 1.7-µm, 75 µm × 250 mm nanoACQUITY UPLC column (35°C). For additional details on UPLC and mass spectrometer conditions see (Goel et al., 2018). The LC-MS/MS data was processed using Proteome Discoverer (v2.1; Thermo Fisher Scientific) and protein identification was carried out using the Mascot search algorithm (Matrix Science). The Scaffold proteome software suite (ver 4.1.1) was used to estimate peptide/peptide groups, resulting in the identification of 21,597 peptide/peptide groups. Differential expression between MON and ORG, was then inferred using the Scaffold 4 Q+ module with default parameters (Precursor Intensity and Centroided Peak Intensity) to infer protein expression levels, using 99.0% minimum and 2 peptides minimum for protein threshold, 95.0% minimum for peptide threshold) and the Mann-Whitney Test for differential expression and FDR < 0.05 as significance levels. The resulting 199 differentially expressed proteins were used for functional annotation and subsequent analysis.

Supplemental References

Amiri, A., Coppola, G., Scuderi, S., Wu, F., Roychowdhury, T., Liu, F., Pochareddy, S., Shin, Y., Safi, A., Song, L., *et al.* (2018). Transcriptome and epigenome landscape of human cortical development modeled in organoids. Science *362*.

de la Torre-Ubieta, L., Stein, J.L., Won, H., Opland, C.K., Liang, D., Lu, D., and Geschwind, D.H. (2018). The Dynamic Landscape of Open Chromatin during Human Cortical Neurogenesis. Cell *172*, 289-304 e218.

Goel, R.K., Meyer, M., Paczkowska, M., Reimand, J., Vizeacoumar, F., Vizeacoumar, F., Lam, T.T., and Lukong, K.E. (2018). Global phosphoproteomic analysis identifies SRMS-regulated secondary signaling intermediates. Proteome Sci *16*, 16.

Harrow, J., Frankish, A., Gonzalez, J.M., Tapanari, E., Diekhans, M., Kokocinski, F., Aken, B.L., Barrell, D., Zadissa, A., Searle, S., *et al.* (2012). GENCODE: the reference human genome annotation for The ENCODE Project. Genome Res *22*, 1760-1774.

Hu, J.S., Vogt, D., Sandberg, M., and Rubenstein, J.L. (2017). Cortical interneuron development: a tale of time and space. Development *144*, 3867-3878.

Johnson, M.B., Wang, P.P., Atabay, K.D., Murphy, E.A., Doan, R.N., Hecht, J.L., and Walsh, C.A. (2015). Single-cell analysis reveals transcriptional heterogeneity of neural progenitors in human cortex. Nat Neurosci *18*, 637-646.

Kamburov, A., Pentchev, K., Galicka, H., Wierling, C., Lehrach, H., and Herwig, R. (2011). ConsensusPathDB: toward a more complete picture of cell biology. Nucleic Acids Res *39*, D712-717.

Kang, H.J., Kawasawa, Y.I., Cheng, F., Zhu, Y., Xu, X., Li, M., Sousa, A.M., Pletikos, M., Meyer, K.A., Sedmak, G., *et al.* (2011). Spatio-temporal transcriptome of the human brain. Nature *478*, 483-489.

Kuleshov, M.V., Jones, M.R., Rouillard, A.D., Fernandez, N.F., Duan, Q., Wang, Z., Koplev, S., Jenkins, S.L., Jagodnik, K.M., Lachmann, A., *et al.* (2016). Enrichr: a comprehensive gene set enrichment analysis web server 2016 update. Nucleic Acids Res *44*, W90-97.

Langfelder, P., and Horvath, S. (2008). WGCNA: an R package for weighted correlation network analysis. BMC Bioinformatics *9*, 559.

Liberzon, A., Subramanian, A., Pinchback, R., Thorvaldsdottir, H., Tamayo, P., and Mesirov, J.P. (2011). Molecular signatures database (MSigDB) 3.0. Bioinformatics *27*, 1739-1740.

Mariani, J., Coppola, G., Zhang, P., Abyzov, A., Provini, L., Tomasini, L., Amenduni, M., Szekely, A., Palejev, D., Wilson, M., *et al.* (2015). FOXG1-Dependent Dysregulation of GABA/Glutamate Neuron Differentiation in Autism Spectrum Disorders. Cell *162*, 375-390.

Nowakowski, T.J., Bhaduri, A., Pollen, A.A., Alvarado, B., Mostajo-Radji, M.A., Di Lullo, E., Haeussler, M., Sandoval-Espinosa, C., Liu, S.J., Velmeshev, D., *et al.* (2017). Spatiotemporal gene expression trajectories reveal developmental hierarchies of the human cortex. Science *358*, 1318-1323.

Pollen, A.A., Nowakowski, T.J., Shuga, J., Wang, X., Leyrat, A.A., Lui, J.H., Li, N., Szpankowski, L., Fowler, B., Chen, P., *et al.* (2014). Low-coverage single-cell mRNA sequencing reveals cellular heterogeneity and activated signaling pathways in developing cerebral cortex. Nat Biotechnol.

Quinlan, A.R., and Hall, I.M. (2010). BEDTools: a flexible suite of utilities for comparing genomic features. Bioinformatics *26*, 841-842.

Rigamonti, A., Repetti, G.G., Sun, C., Price, F.D., Reny, D.C., Rapino, F., Weisinger, K., Benkler, C., Peterson, Q.P., Davidow, L.S., *et al.* (2016). Large-Scale Production of Mature Neurons from Human Pluripotent Stem Cells in a Three-Dimensional Suspension Culture System. Stem cell reports *6*, 993-1008.

Robinson, M.D., McCarthy, D.J., and Smyth, G.K. (2010). edgeR: a Bioconductor package for differential expression analysis of digital gene expression data. Bioinformatics *26*, 139-140.

Schindelin, J., Arganda-Carreras, I., Frise, E., Kaynig, V., Longair, M., Pietzsch, T., Preibisch, S., Rueden, C., Saalfeld, S., Schmid, B., *et al.* (2012). Fiji: an open-source platform for biological-image analysis. Nat Methods *9*, 676-682.

Scuderi, S., D'Amico, A.G., Castorina, A., Imbesi, R., Carnazza, M.L., and D'Agata, V. (2013). Ameliorative effect of PACAP and VIP against increased permeability in a model of outer blood retinal barrier dysfunction. Peptides *39*, 119-124.

Subramanian, A., Tamayo, P., Mootha, V.K., Mukherjee, S., Ebert, B.L., Gillette, M.A., Paulovich, A., Pomeroy, S.L., Golub, T.R., Lander, E.S., *et al.* (2005). Gene set enrichment analysis: a knowledge-based approach for interpreting genome-wide expression profiles. Proc Natl Acad Sci U S A *102*, 15545-15550.

Thomsen, E.R., Mich, J.K., Yao, Z., Hodge, R.D., Doyle, A.M., Jang, S., Shehata, S.I., Nelson, A.M., Shapovalova, N.V., Levi, B.P.*, et al.* (2016). Fixed single-cell transcriptomic characterization of human radial glial diversity. Nat Methods *13*, 87-93.

Figure S1 (Related to Figure 1).

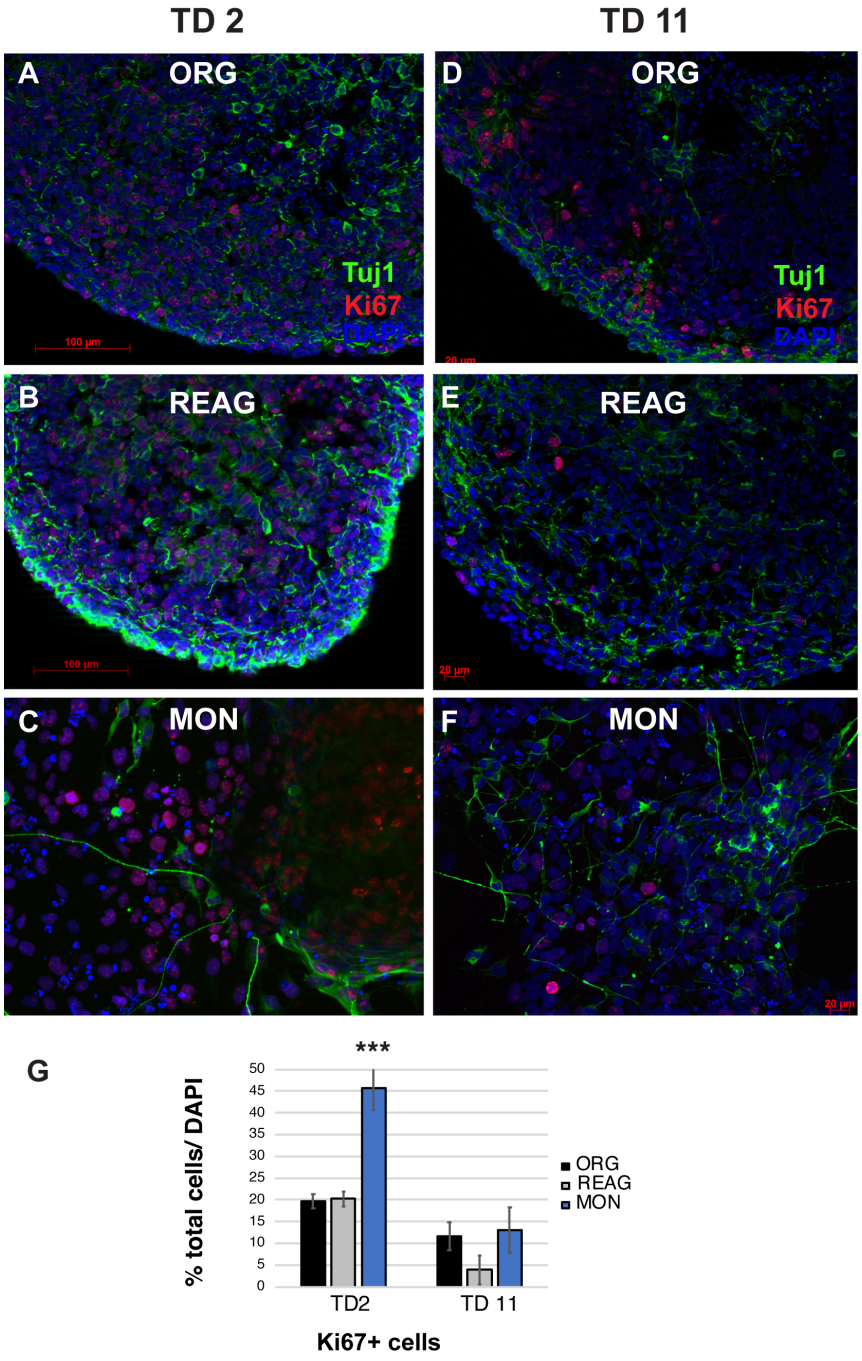

Figure S1. A-F, Representative images of immunocytochemical staining with the proliferative marker Ki67 and the neuron-specific class TUJ1 in ORG, REAG and MON preparations at TD 2 (**A-C**) and TD 11 (**D-F**). G, Proportion of $Ki67^+$ cells by stereological quantification over $DAPI^+$ nuclei. Results in (**G**) are the mean± SEM of n=3 biologically different iPSC lines per condition (ORG, REAG, MON) differentiated in parallel (one preparation each). For each preparation, 3 technical replicates (individual organoids, reaggregates or tissue culture wells) were analyzed. ***$p<0.001$ analyzed by Student's t-test, two tailed. Related to **Figure 1**.

Figure S2 (Related to Figure 3 and Table S4).

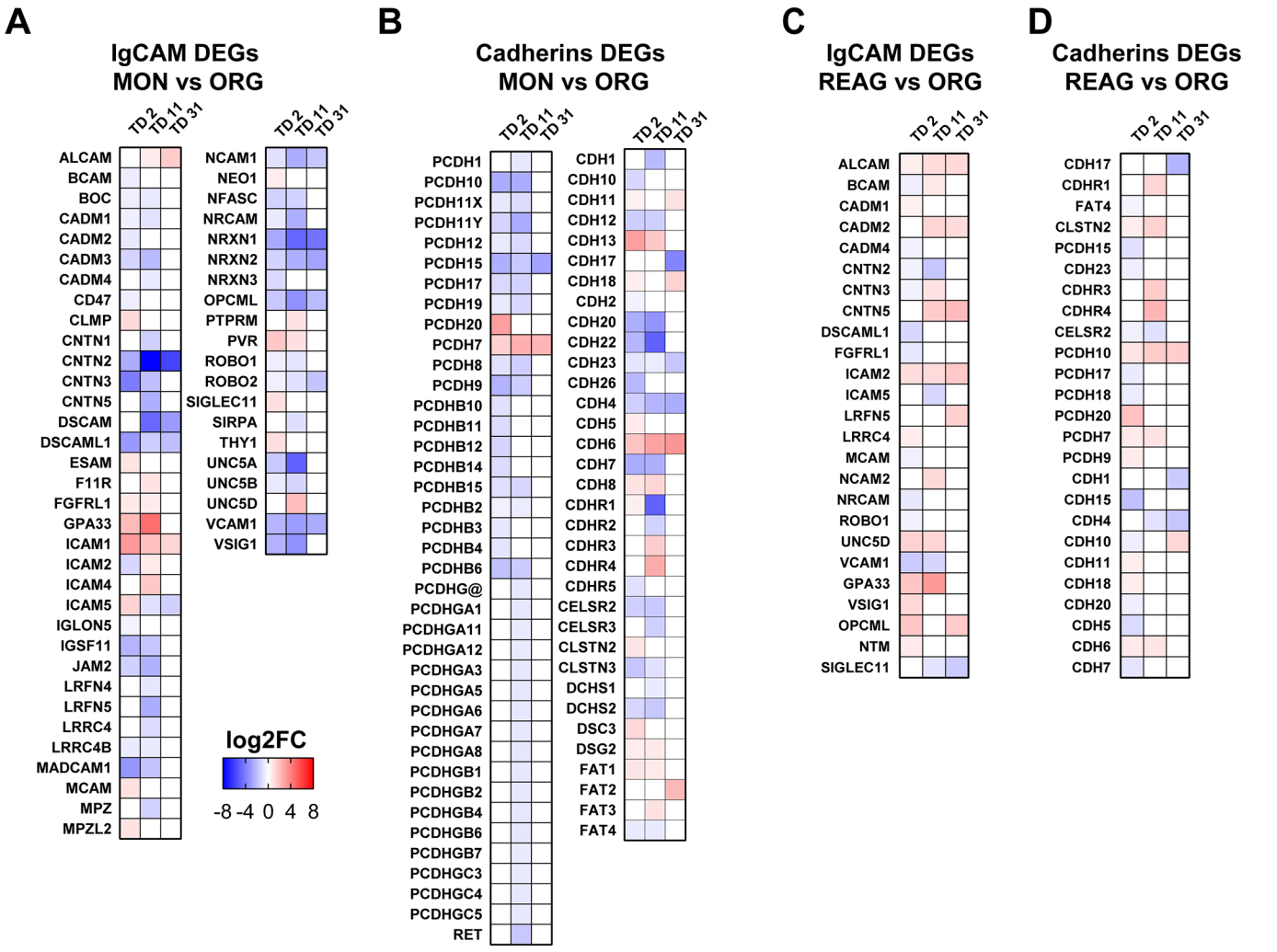

Figure S2. (A-D) Heat map of genes in the *Cell Adhesion* sublist (Table S4b) exhibiting differential gene expression (log2 fold change values, FDR<0.05) between MON and ORG (A-B), or between REAG vs ORG (C-D) at least at one time point analyzed. Related to **Figure 3** and **Table S4.**

Figure S3 (Related to Figure 3 and Table S4).

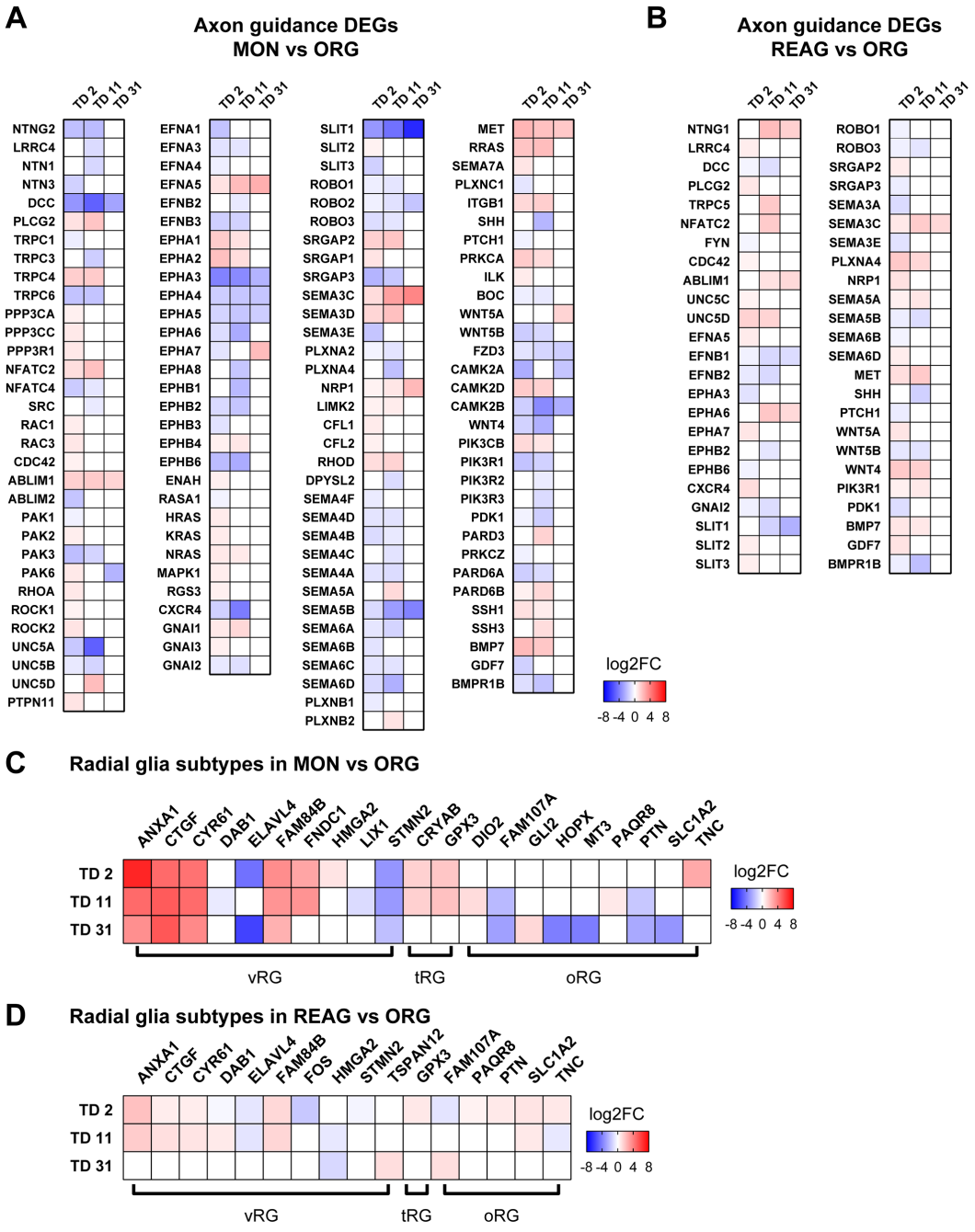

Figure S3. (A-B) Heat map of genes in the *Axon guidance* sublist (**Table S4b**) differentially expressed (log2 fold change values, FDR<0.05) between MON vs ORG (A) and REAG vs ORG (B) at least at one time point analyzed. **C-D**) Heat map of genes that identify radial glial subtypes (vRG, ventricular radial glia; tRG, truncated radial glia; oRG, outer radial glia) differentially expressed (log2 fold change values, FDR<0.05) between MONvsORG and between REAGvsORG, at least at one time point (**TableS4a**). Related to **Figure 3** and **Table S4**.

Figure S4 (Related to Figure 4 and Table S4).

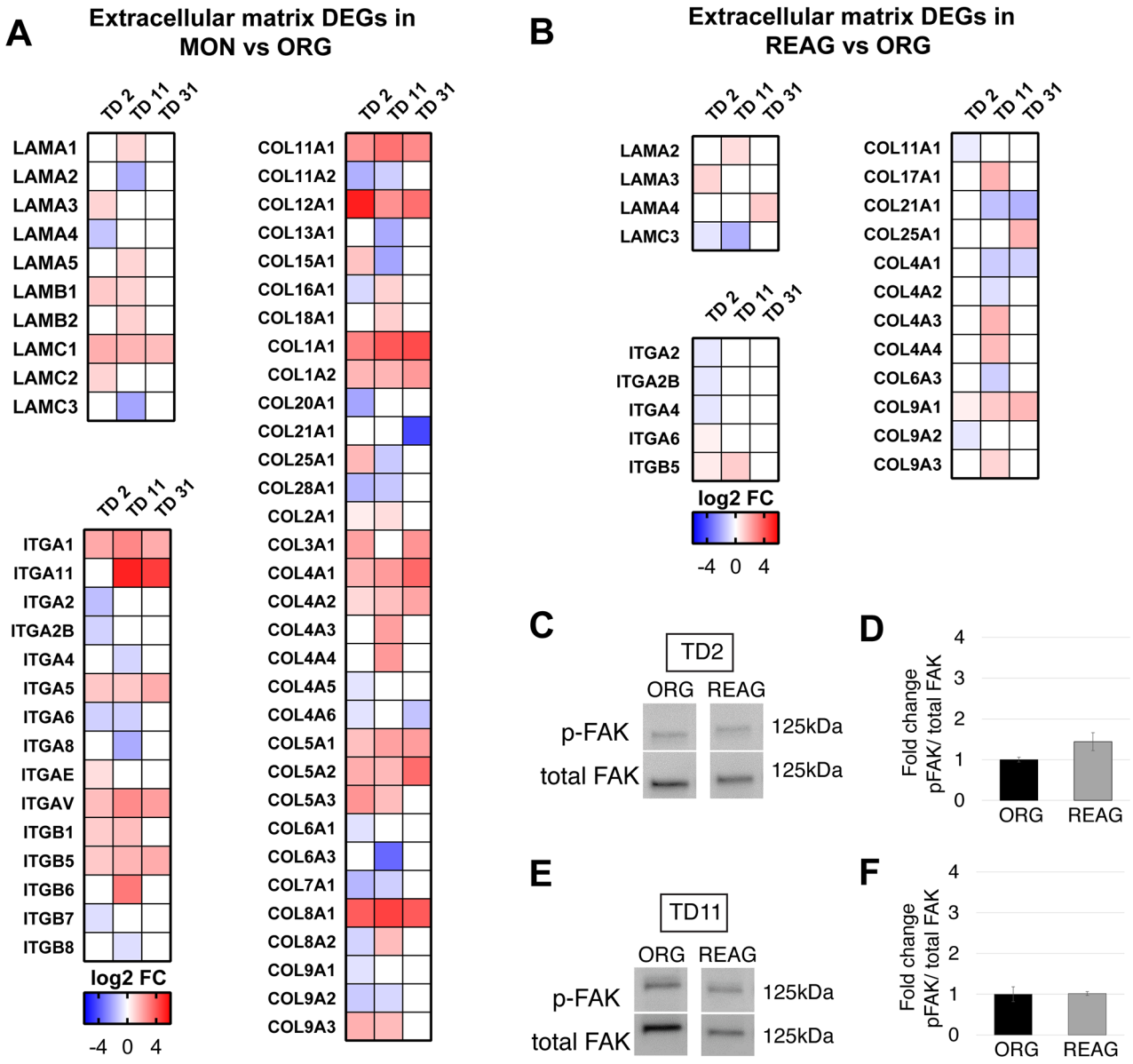

Figure S4. (A-B) Heat map of genes in the *Extracellular matrix* sublist (**Table S4d**) differentially expressed (log2 fold change values, FDR<0.05) between MON and ORG (A), or REAG vs ORG (B) at least at one time point analyzed. (**C-F**) Western blot analysis of phospho-FAK over total FAK protein expression in ORG and REAG at TD2 and TD11. Related to **Figure 4** and **Table S4**.

Figure S5 (Related to Figure 6).

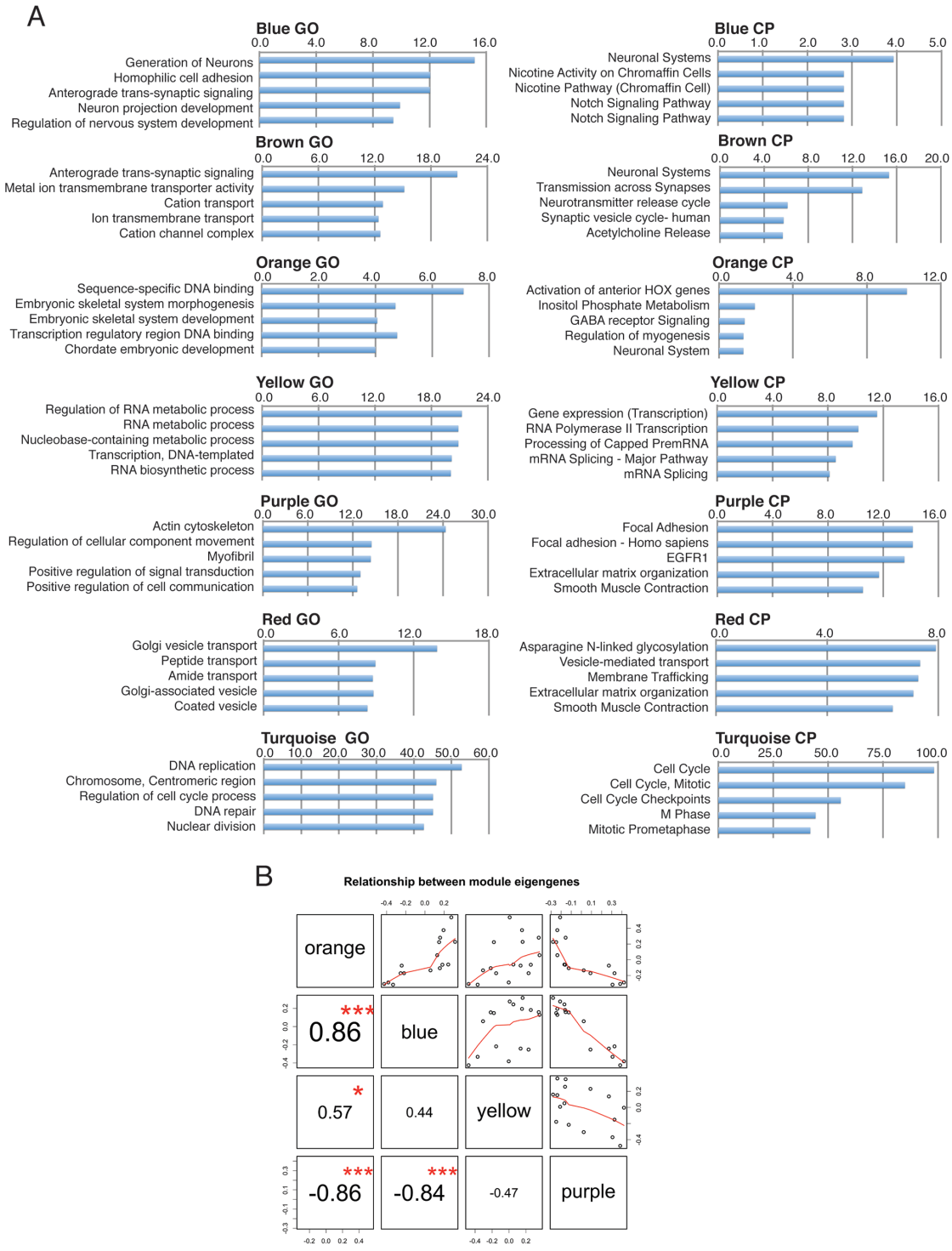

Figure S5. Characterization of the seven co-expression modules differentially expressed between ORG and MON. (**A**) Barplots of corrected p-values (expressed as –log10) for the top 5 Gene Ontologies (left) and Canonical Pathways (right) annotations. (**B**) Module to module eigenvalue correlation plots. Shown are the correlation coefficients and the associated significance. Related to **Figure 6**.

Figure S6 (Related to Figure 7).

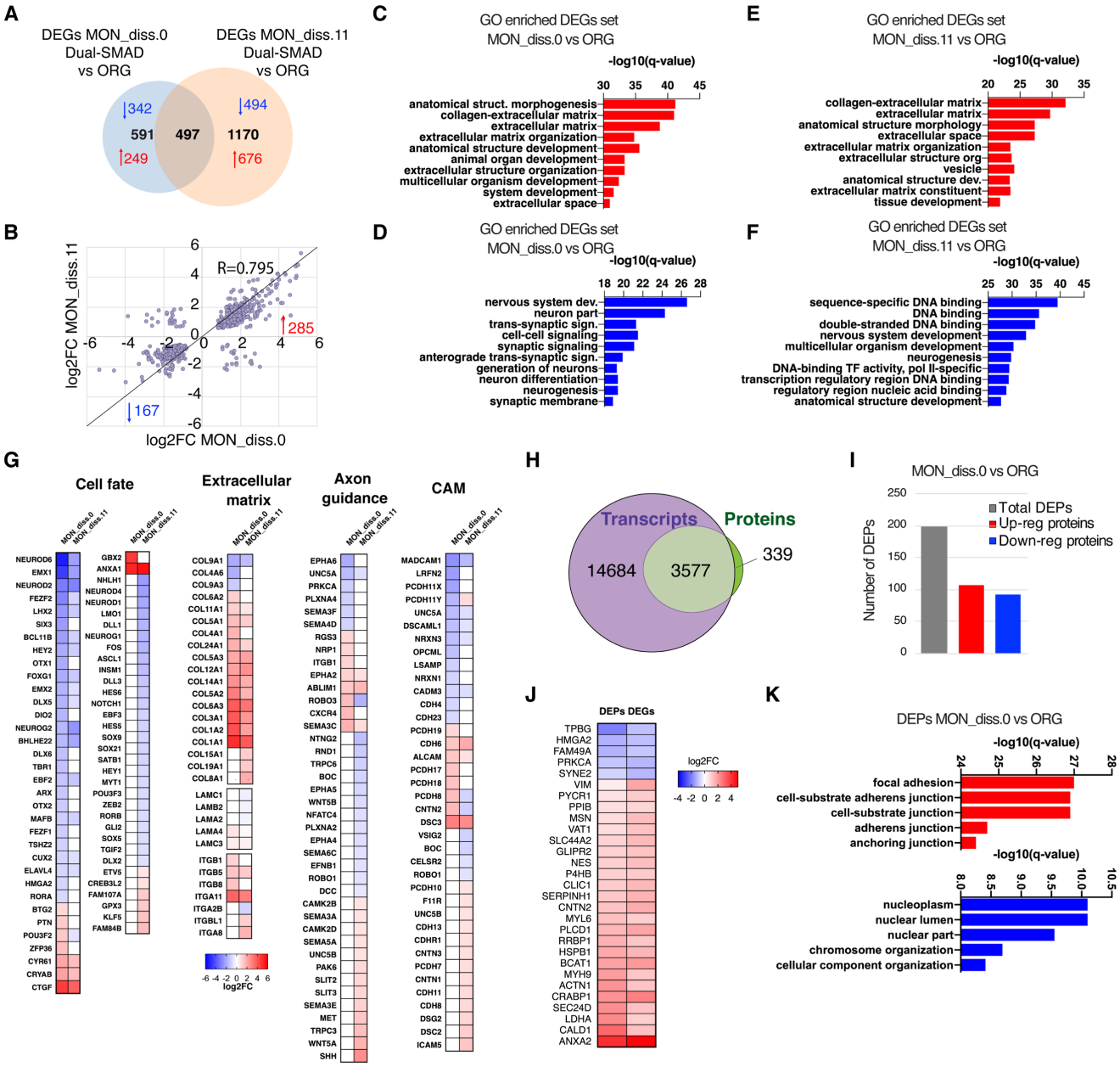

Figure S6. Consistency of transcriptomic changes in MON compared to ORG culture systems across different times of dissociation. (**A**) Venn diagram of total number of DEGs in early and late dissociated MON vs ORG. (**B**) Correlation plot of the shared DEGs in MON_diss.0 and MON_diss.11 compared to ORG. (**C-F**) Top GO-enrichment terms for up-regulated (red, C,E) and downregulated (blue, D,F) genes in early dissociated MON (C,D) and late dissociated MON (E,F). (**G**) Heat map of genes in the *neurodevelopmental genes list* differentially expressed (log2 fold change values, FDR<0.05) in MON_diss.0 and MON_diss_11 vs ORG. (**H**) Representation of the coverage and overlap between total identified transcripts and proteins in MON_diss.0 and ORG at TD25. (**I**) Number of differentially expressed proteins (DEPs) in MON_diss.0 vs ORG. (**J**) Heatmap of convergent DEPs and DEGs (log2 fold change values, FDR<0.05). (**K**) Top GO-enrichment terms for up- or down-regulated proteins in MON. Related to **Figure 7, Table S8.**

Supplemental Tables (uploaded as separate excel files)

Table S1. Metadata: list of all samples and experiments.
Table S2. Differential gene expression (DGE) analysis between time points in MON and ORG.
Table S3. Differential gene expression (DGE) analysis between MON and ORG at three time points, TD2, TD11 and TD31. Primer sequences used for qPCR validation of RNAseq data analysis.
Table S4. Neurodevelopmental genes list.
Table S5. Differential gene expression (DGE) analysis between REAG and ORG at three time points, TD2, TD11 and TD31.
Table S6. WGCNA analysis in MON and ORG samples at TD2, TD11 and TD31
Table S7. Transcription Factors Analysis results for the Blue module.
Table S8. Differential gene expression (DGE) analysis between early dissociated conditions (MON, REAG) and ORG, and late dissociated conditions (MON, REAG) and ORG at TD25. Proteomic analysis by LC MS/MS in early dissociated MON and ORG at TD25